Journal of Physics: Condensed Matter

https://iopscience.iop.org/journal/0953-8984

Impact factor = 2.333

Accepted January 24th 2022

Electroosmotic modulated unsteady squeezing flow with temperature-dependent thermal conductivity, electric and magnetic field effects

[1]J. Prakash, *[2]Dharmendra Tripathi, [3]O. Anwar Bég and [4]Ravi Kumar Sharma

[1]*Department of Mathematics, Avvaiyar Government College for Women, Karaikal – 609 602, U.T of Puducherry, **India**.*

[2]*Department of Mathematics, National Institute of Technology Uttarakhand, Srinagar– 246174, India.*

[3]*Multi-Physical Engineering Sciences Group, Dept. Mechanical and Aeronautical Engineering, SEE, Salford University, Manchester, M54WT, **UK**.*

[4]*Department of Mechanical Engineering, Manipal University Jaipur, Rajasthan, 303007, **India**.*

Corresponding author: dtripathi@nituk.ac.in

Abstract

Modern lubrication systems are increasingly deploying smart (functional) materials. These respond to various external stimuli including electrical and magnetic fields, acoustics, light etc. Motivated by such developments, in the present article unsteady electro-magnetohydrodynamics (EMHD) squeezing flow and heat transfer in a smart ionic viscous fluid intercalated between parallel plates with zeta potential effects is examined. The proposed mathematical model of problem is formulated as a system of partial differential equations (continuity, momenta and energy). Viscous dissipation and variable thermal conductivity effects are included. Axial electrical distribution is also addressed. The governing equations are converted into ordinary differential equations via similarity transformations and then solved numerically with MATLAB software. The transport phenomena are scrutinized for both when the plates move apart or when they approach each other. Also, the impact of different parameters such squeezing number, variable thermal conductivity parameter, Prandtl number, Hartmann number, Eckert number, zeta potential parameter, electric field parameter and electroosmosis parameter on the axial velocity and fluid temperature are analyzed. For varied intensities of applied plate motion, the electro-viscous effects derived from electric double-capacity flow field distortions are thoroughly studied. It has been shown that the results from the current model differ significantly from those achieved by using a standard Poisson-Boltzmann equation model. Axial velocity acceleration is induced with negative squeeze number (plates approaching, $S< 0$) in comparison to that of positive squeeze number (plates separating, $S>0$). Velocity enhances with increasing electroosmosis parameter and zeta potential parameter. With rising values of zeta potential and electroosmosis parameter, there is a decrease in temperatures for $U_e > 0$ for both approaching i. e. squeezing plates ($S < 0$) and separating ($S > 0$) cases. The simulations provide novel insights into smart squeezing lubrication with thermal effects and also a solid benchmark for further computational fluid dynamics (CFD) investigations.

Keywords: *Smart lubricants; Squeezing flow; Magnetic field; Electroosmotic flow; Zeta potential; Thermal Conductivity; Nusselt number*

Nomenclature

a - characteristic frequency parameter (1/s)
B_0 - Uniform magnetic field (Tesla)
c_p- specific heat at constant pressure (J kg^{-1} K^{-1})
e – electron charge (C) ($kg^{1/2}\, m\, \Omega^{-1/2}\, sec^{-1/2}$)
E_X- axial electric body force term (V m $^{-1}$)
Ec – Eckert number (-)
f - dimensionless velocity (-)
$\tilde{h}(\tilde{t})$- Distance between parallel plates (m)
$\tilde{H}$- Initial position of plate (m)
Ha - Hartmann number (-)
k_B- Boltzmann constant (V m^{-1}) ($kgm^2\, sec^{-2}\, Kelvin^{-1}$)
m - electroosmosis parameter
$\tilde{n}_0$- ion density (m^{-3})
$\tilde{P}$- dimensional pressure (Pa)
Pr – Prandtl number (-)
S – Squeezing number (-)
$\tilde{T}_{\tilde{H}}$- parallel plate-fluid difference temperature (K)
$\tilde{T}$- dimensional fluid temperature (K)
$\tilde{t}$- dimensional time (s)
$(\tilde{U}, \tilde{V})$- velocity (m s^{-1}) in the direction of $(\tilde{X}, \tilde{Y})$ (m)
U_e - dimensionless electric field parameter (-)
U_{HS} - Helmholtz-Smoluchowski velocity (m/s)
$\tilde{z}$ – valence (-)

Greek letter

ε - variable thermal conductivity (VTC) parameter (-)
ε_{ef}- electrical permittivity of the lubricant (C V^{-1} m^{-1}) ($m^{-1}\, \Omega^{-1}\, sec$)
$\bar{\kappa}$ - thermal conductivity of the electromagnetic viscous lubricant (W m $^{-1}$ K^{-1})
κ - Debye-Hückel parameter
θ - dimensionless fluid temperature (-)
$\tilde{\Phi}$ electric potential (Vm^{-1})
Φ - dimensionless electric potential (-)
$\tilde{\rho}_e$ - net charge number density (C m^{-3})
ρ - fluid density (kg m^{-3})
μ dynamic viscosity ($kg\, m^{-1}\, sec^{-1}$)
σ - electrical conductivity (S m^{-1}) ($\Omega^{-1}\, m^{-1}$)
ξ - zeta potential parameter
η - dimensionless axial coordinate (-)

δ - dimensionless length (-)

1. INTRODUCTION

In modern tribological systems, the flow of viscous fluid (lubricant) squeezed between two parallel plates features frequently [1]. This regime is critical in sustaining efficient motion of moving parts in many engineering applications including jet engines, earthquake dampers, landing gear, locomotive bearing systems and manufacturing. Squeezing lubrication flows also provide an excellent motivation for analytical and numerical studies since with appropriate scaling, the conservation equations can be reduced to ordinary differential boundary value problems and inertial effects may be often neglected. These provide an important compliment to experimental investigations. Many excellent theoretical studies of squeezing flow have been reported for both Newtonian fluid [2 & 3] and also non-Newtonian fluid [4 & 5]. In particular, squeeze flow models provide a quantification of the *load-bearing capacity* [6]. In squeezing hydrodynamics, unsteady effects may also arise. Several workers have addressed such aspects. Chandrasekharan and Ramanaiah [7] examined theoretically the time-dependent viscous squeezing flow between rectangular plates and between circular plates, where the lower plate is fixed and the upper plate moves towards the lower plate. They derived the pressure distribution as a function of the film thickness and velocity of the upper plate, including inertia effects. Bhattacharjee and Das [8] computed the unsteady two-dimensional flow of dusty fluids between two circular plates, one fixed and the other in unsteady motion. They evaluated the dust particles on the variable load capacity and showed that pressure gradient is elevated.

The above studies were confined to *electrically non-conducting* lubricants. However, for a number of decades, engineers have established that magnetic lubricants provide considerable advantages to conventional tribological fluids, since they can be manipulated by external magnetic fields, and this can increase the load carrying capacity of the lubricant. Pioneering work in magnetic squeezing films was conducted by Hughes [9] who showed that bearing pressurization and load capacity are enhanced in journal, thrust and also slider bearings, with judicious selection of external magnetic field and careful electrode design of the bearing plates under open circuit conditions. The analysis of magnetic squeezing films requires *magnetohydrodynamics* (MHD) in which the Navier-Stokes viscous flow model is augmented with appropriate magnetic body force terms. Many researchers have explored novel configurations for magnetic tribological flows owing to recent developments in more stable magnetic suspensions which are finding applications in steel-steel sliding damper applications [10], spacecraft landing gear and seismic isolation devices [11], multi-stage magnetic fluid seal systems [12] and rocket turbo pump seals [13]. Naduvinamani *et al.* [14] studied analytically the influence of static axial magnetic field and surface roughness on the couple stress magnetized lubricant squeeze film between circular stepped plates. They derived a modified averaged Reynolds magnetic lubrication equation and computed the mean squeeze film pressure, load carrying capacity and squeeze film time, observing that stronger magnetic field elevates the load carrying capacity and beneficially delays the time of approach as compared, achieving superior performance to non-magnetic lubricants. Umavathi *et al.* [15] used a finite difference method in the MATLAB bvp4c solver based on Lobotto quadrature, to simulate the transient squeezing flow of magnetized nanofluid lubricant between parallel disks with mixed boundary conditions. They noted that in the central zone, greater resistive magnetic body force (i.e. stronger Hartmann number) strongly damps velocity and also nanoparticles mitigate heat build-up in squeeze films, effectively aiding against corrosion and plate inner surface degradation. They also found that unequal Biot numbers induce substantial cooling of the regime for both cases of disk suction or injection, identifying that Robin (mixed) boundary conditions produce significantly different results compared with conventional thermal boundary conditions. Chu et al. [16] studied the squeezing magneto-elastohydrodynamic lubrication (MEHL) motion of circular contacts under transverse magnetic field with a constant load condition. They demonstrated that elevation in magnetic field intensity serves to successfully boost the effective lubricant viscosity, and favorably influences the pressure distribution and film shape and delays approach times. Shah and Shah [17] used the Shliomis ferrofluid flow model (SFFM) to investigate ferromagnetic circular squeeze film flow under an oblique radially variable magnetic field (VMF) with momentum slip at the film– porous interface and rotations of both the discs. Further investigations of magnetohydrodynamic squeeze film dynamics include Prajapati [18] and Khan *et al.* [19] (who deployed a Variation of Parameters Method (VPM) to compute the load capacity of magnetic squeezing films). These studies all confirmed that magnetic lubricants controls the variation of lubricant viscosity under certain extreme operating conditions and achieve improved efficiency.

Thermal effects can also be significant in squeezing lubrication flows and can lead to degradation of the plates (bearing surfaces), corrosion, surface wear etc. Heat transfer in such systems has therefore also received some attention, both for magnetic and non-magnetic situations. Çelika *et* *al.* [21] used a Gegenbauer Wavelet Collocation Method to study heat transfer in the squeezing flows between parallel disks (one impermeable and the other porous) under magnetic field. They computed the influence of squeeze number, Hartmann number and suction/blowing disk parameter on velocity and temperature evolution. Hayat *et al.* [21] used Liao's homotopy analysis method (HAM) and the Cattaneo-Christov heat flux model to analyse the axisymmetric squeezing flow of a viscoelastic second grade fluid between two parallel plates. They showed that thermal relaxation effects reduce the temperature compared with the conventional Fourier heat conduction model whereas positive squeezing (plates separating) elevates temperatures. Shamshuddin *et al.* [22] studied gryotactic bioconvection and chemical reaction effects under strong magnetic fields in unsteady squeezing flow and heat transfer. Khan *et al.* [23] examined variable thermal conductivity and non-Newtonian effects in thermal squeezing flow in a sensor configuration. Further studies include Su and Yin [24] (on inclined magnetic field effects on the unsteady squeezing flow between parallel plates with wall mass flux) and Mishra *et al*. [25] (who considered mass diffusion and Cattaneo-Christov heat flux effects in magnetic squeezing flow in a Riga dual plate system).

Another mechanism of smart lubrication is the implementation of *electrical fields* in conjunction with ionic liquids [26] which are increasingly being deployed as tribological media. These experience electro-viscous effects and are termed electro-osmotic flows. Electroosmosis is an electrokinetic phenomenon induced by Coulomb electrical force and influenced by the electric potential across a porous material, capillary tube, microchannel, or on charged surfaces (plates). In small channels, electroosmotic flow may also be deployed in chemical separation techniques, notably capillary electrophoresis. Several investigations of heat transfer in electro-osmotic flows have been reported [27, 28]. Electroosmotic squeezing flows have also recently been studied by several investigators. Zhao *et al.* [29] investigated theoretically the electro-viscous effect in the squeezing flow of thin electrolyte films confined between two curved and flat charged surfaces with lubrication approximations. They solved the Nernst–Planck–Poisson/Navier–Stokes equation and explored the interplay between conservative electric double layer (EDL) force and electroviscous-effect-enhanced dissipative hydrodynamic force, showing that the counter-ion conductivity of the EDL strongly influences the electro-viscous effect under a given zeta potential and also produces much sharper velocity profiles. Bike *et al.* [30] considered electro-kinetic squeezing and sliding motion lubrication flows, deriving a general differential equation for the streaming potential showing that electrokinetic lift may induce detachment by shear of particles from the solid surfaces. Talapatra and Chakraborty [31] studied the effects of distortion of the electric double layer flow field on electro-osmotic squeezing flow between two charged parallel plates. They noted that for squeezing flow occurs, due to the extremely confined geometry, the instantaneous liquid layer thickness is of the same or less order than characteristic electric double layer thickness, leading to a depletion in counterions within the bulk liquid due to an excess accumulation of those in the electrical double layer. Squeezing rates were also shown to have a significant influence on velocity and ionic distribution. Additional works considering electro-kinetic squeezing flows include Bo and Umehara [32] (who considered very thin water film lubrication of ceramics) and Liu *et al*. [33] (who addressed electrical dissipation in aqueous electrolyte films with overlapping electric double layers).

The above studies were confined to either *ionic electro-osmotic squeezing flows* or *magnetohydrodynamics (MHD) squeezing flows*. In recent years, engineers have explored the *combination of electrical and magnetic fields* in transport phenomena. Many areas have been explored including electromagnetic nanofluid duct flow optimization [34], microchannel electro-osmotic hydromagnetic flows [35] and rotating thermo-magnetic electro-osmotic flow [36]. Ramesh *et al.* [37] investigated the combined electro-osmotic and magnetohydrodynamics peristaltic slip flow of a dusty Jeffrey fluid in a wavy asymmetric microchannel, under static transverse magnetic field and axial electric field. Slip effects are considered to examine the flow behavior.

Very few studies however have examined combined *electro-magneto-hydrodynamic (EMHD) squeezing flows*. A new family of lubricants known as magnetic ionic lubricants [38] has emerged which combine magnetohydrodynamics and electro-osmotic phenomena to allow enhanced functionality of lubricants. Lorentz body force encountered in magnetohydrodynamics can be simultaneously considered as a control mechanism with electro-osmotic body force and electrical double layer effects associated with electro-kinetics. Important studies in this regard include Bombard *et al.* [39] in steel-polymeric point contact mechanics and Okabe *et al*. [40] for vacuum-compatible non-contact seals. Of the rare investigations on EMHD squeezing flows, Thumma *et al.* [41] employed a spectral local linearization method (SLLM) to simulate the unsteady magnetic ionic lubrication in squeezing flows with radiative flux in an electromagnetic actuator. They also included species (mass) diffusion and heat generation/absorption and destructive species homogeneous reaction effects in their model. They observed that velocity and temperature are elevated with greater squeezing and heat source parameters, the flow is damped with magnetic parameter (Hartmann number) whereas electro-osmotic parameter accelerates the flow and suppresses temperatures. Correspondingly, momentum enhances at lower plate and detracts with rise in modified Hartmann number.

Viscous heating and zeta potential effects were both ignored in [41]. In the present work, a mathematical model is therefore developed for the combined magnetohydrodynamics and electro-osmotic squeezing flow and heat transfer *with zeta potential, viscous heating and variable thermal conductivity effects* in parallel plate lubrication geometry. The resulting *electro-magnetic-hydrodynamics viscous squeezing flow with dissipation effects* has to the authors' knowledge not been considered thus far in the scientific literature. In particular, there is limited literature, dealing with thermo-osmotic effects in squeezing flows which provides strong motivation for the present work. The transformed boundary value problem is solved with MATLAB software. Extensive computations are performed for the effects of key parameters (e. g. squeezing parameter, Eckert number, electro-osmotic parameter, zeta potential parameter, Hartmann number etc.) on velocity, temperature and Nusselt number. The external magnetic and electrical body forces are shown to be able to provide a dual mechanism for controlling the heat transfer and flow dynamics in squeezing flows. Both approaching plate and separating plate scenarios are studied.

2. ELECTROMAGNETIC SQUEEZE TRANSPORT MODEL FORMULATION

Two-dimensional unsteady, incompressible, viscous, electro-osmotic magnetic ionic squeezing fluid flow and heat transmission is studied in a parallel plate lubrication system, as a model of smart (functional) tribology. The physical model is visualized in **Fig. 1**. A Cartesian coordinate system $(\tilde{X}, \tilde{Y})$is considered with the $\tilde{X}$-axis directed along the plate and the $\tilde{Y}$ axis perpendicular to it. In the magnetic ionic lubricant, suspended particles are subjected to time-varying transverse magnetic field, $\tilde{B}(\tilde{t})$, and axial electrical field $\tilde{E}_{\tilde{X}}(\tilde{t})$. The thin film flow possesses fluid electrical net charge thickness $\tilde{\rho}_e$ and variable thermal conductivity $\tilde{\kappa}(\tilde{T})$. Only axial electro-osmotic and Lorentz magnetic body forces are invoked. All other body forces are disregarded. The gap between the parallel plates is given by:

$$\tilde{h}(t) = \tilde{H}(1 - a\tilde{t})^{1/2}, \tag{1}$$

Here the preliminary position of the upper plate is $\widetilde{H}$ at $\tilde{t} = 0$ and a is a characteristic frequency parameter. In this model, the following assumptions are invoked:

1) No chemical reaction or radiative heat transfer,
2) the fluid is incompressible,
3) a horizontal parallel plate channel is considered
4) no slip occurs at the plate wall internal surfaces
5) the induced magnetic field is expected to be insignificant since the magnetic Reynolds number of the flow is believed to be extremely small.
6) All additional body forces are ignored.

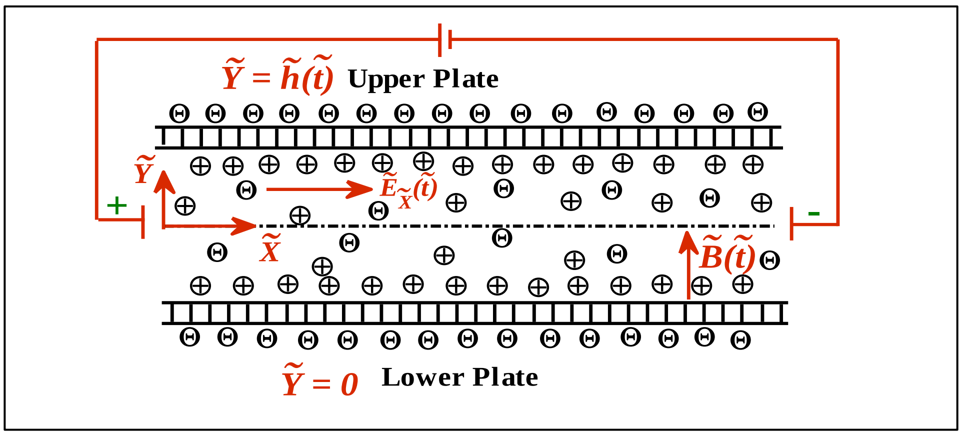

Figure 1: Geometrical representation of the electromagnetic squeezing flow regime.

2.1 The governing equations

The magnetic ionic lubricant squeezing flow is governed by the modified continuity, momentum and energy equations as:

$$\frac{\partial \tilde{U}}{\partial \tilde{X}} + \frac{\partial \tilde{V}}{\partial \tilde{Y}} = 0, \tag{2}$$

$$\rho\left(\frac{\partial \tilde{U}}{\partial \tilde{t}} + \tilde{U}\frac{\partial \tilde{U}}{\partial \tilde{X}} + \tilde{V}\frac{\partial \tilde{U}}{\partial \tilde{Y}}\right) = -\frac{\partial \tilde{P}}{\partial \tilde{X}} + \mu\left(\frac{\partial^2 \tilde{U}}{\partial \tilde{X}^2} + \frac{\partial^2 \tilde{U}}{\partial \tilde{Y}^2}\right) - \sigma \tilde{B}(\tilde{t})u + \tilde{\rho}_e \tilde{E}_{\tilde{X}}(\tilde{t}), \tag{3}$$

$$\rho\left(\frac{\partial \tilde{V}}{\partial \tilde{t}} + \tilde{U}\frac{\partial \tilde{V}}{\partial \tilde{X}} + \tilde{V}\frac{\partial \tilde{V}}{\partial \tilde{Y}}\right) = -\frac{\partial \tilde{P}}{\partial \tilde{Y}} + \mu\left(\frac{\partial^2 \tilde{V}}{\partial \tilde{X}^2} + \frac{\partial^2 \tilde{V}}{\partial \tilde{Y}}\right), \tag{4}$$

$$\rho c_p\left(\frac{\partial \tilde{T}}{\partial \tilde{t}}+\tilde{U}\frac{\partial \tilde{T}}{\partial \tilde{X}}+\tilde{V}\frac{\partial \tilde{T}}{\partial \tilde{Y}}\right)=\frac{\partial}{\partial \tilde{X}}\left(\tilde{\kappa}(\tilde{T})\frac{\partial \tilde{T}}{\partial \tilde{X}}\right)+\frac{\partial}{\partial \tilde{Y}}\left(\tilde{\kappa}(\tilde{T})\frac{\partial \tilde{T}}{\partial \tilde{Y}}\right) \tag{5}$$

$$+\mu\left(2\left(\left(\frac{\partial \tilde{U}}{\partial \tilde{X}}\right)^2+\left(\frac{\partial \tilde{V}}{\partial \tilde{Y}}\right)^2\right)+\left(\frac{\partial \tilde{U}}{\partial \tilde{Y}}+\frac{\partial \tilde{V}}{\partial \tilde{X}}\right)^2\right)+\sigma\tilde{B}^2(\tilde{t})u^2+\sigma\tilde{E}_{\tilde{X}}^2(\tilde{t}),$$

Here, velocity components $(\tilde{U},\tilde{V})$ correspond to the $(\tilde{X},\tilde{Y})$direction respectively, $\rho$is magnetic ionic fluid density, $\tilde{P}$is pressure, $\mu$is dynamic viscosity, $c_p$specific heat and σ is the electrical conductivity of fluid. Axial applied electric field $\tilde{E}_{\tilde{X}}(\tilde{t})$ is defined as:

$$\tilde{E}_{\tilde{X}}(\tilde{t})=\frac{E_X}{1-a\tilde{t}}, \tag{6}$$

Uniform magntic field is prescribed by the relation:

$$\tilde{B}(\tilde{t})=\frac{B_0}{\sqrt{1-a\tilde{t}}}, \tag{7}$$

Following Seddeek and Salama [42], the temperature-dependent thermal conductivity $\tilde{\kappa}(\tilde{T})$ can be defined as:

$$\tilde{\kappa}=\bar{\kappa}\left(1+\varepsilon\frac{\tilde{T}}{\tilde{T}_{\tilde{H}}}\right), \tag{8}$$

Here $\bar{\kappa}$is the liquid thermal conductivity of the magnetic ionic lubricant, $\tilde{T}_{\tilde{H}}$ is fluid difference temperature across the plate gap (squeezing regime) and $\varepsilon$is a variable thermal conductivity (VTC) parameter. In Eqn. (8), the parameter εcan be derived based on a Taylor expansion as

$$\varepsilon=\left(\frac{\tilde{T}_{\tilde{H}}}{\bar{\kappa}}\right)\left(\frac{\partial\bar{\kappa}}{\partial\tilde{t}}\right)_{\tilde{t}=\tilde{h}}.$$

2.2. Electrical potential

The Boltzmann-Poisson equation is deployed to simulate the distribution of electrical potential between the plates, as a result of the EDL, and takes the form:

$$\nabla^2\bar{\Phi}=-\frac{\bar{\rho_e}}{\varepsilon_{ef}}, \tag{9}$$

where ε_{ef} is the permittivity or the dielectric constant of the magnetic ionic fluid (magnetic electrolytic solution). The *count of the ions of type-i*, referred to as n_i, in a symmetric magneto-electrolytic solution can be assumed to follow the equilibrium Boltzmann distribution equation:

$$\tilde{n}_i = \tilde{n}_{i0}\, exp\left(-\frac{\tilde{z}_i e\tilde{\Phi}}{k_B \tilde{T}_{\tilde{H}}}\right). \tag{10}$$

Here $\tilde{T}_{\tilde{H}}$, e , k_B, $\tilde{n}_{i0}$ and $\tilde{z}_i$ designate the absolute temperature, charge of an electron, Boltzmann constant, bulk ionic concentration and the valence of type-i ions, respectively.

The net volume charging density ($\tilde{\rho}_e$) is linked to the overall concentration difference between anions and cations for a symmetric magneto-electrolytic solution of value $\tilde{z}$, as follows:

$$\tilde{\rho}_e = \tilde{z}e(\tilde{n}_+ - \tilde{n}_-). \tag{11}$$

Implementing Eqn. (10) for the value of the numbers of each ion, in Eqn. (11) as seen below:

$$\tilde{\rho}_e = -2\tilde{z}e\tilde{n}_0\, sinh\left(\frac{\tilde{z}e\tilde{\Phi}}{k_B \tilde{T}_{\tilde{H}}}\right). \tag{12}$$

Substituting the value of charge density (Eqn. (12)) in the Boltzmann-Poisson equation (Eqn. (9)) the following second order differential equation emerges for electrical potential distribution, $\tilde{\Phi}$:

$$\tilde{\rho}_e = -2\tilde{z}e\tilde{n}_0\, sinh\left(\frac{\tilde{z}e\tilde{\Phi}}{k_B \tilde{T}_{\tilde{H}}}\right), \tag{13}$$

2.3 Dimensional Boundary conditions

The imposed boundary conditions for the proposed problem at the upper and lower plates are defined by:

$$\begin{gathered} \tilde{U} = 0, \tilde{V} = \frac{d\tilde{h}}{d\tilde{t}}, \tilde{T} = \tilde{T}_{\tilde{H}}, \tilde{\Phi} = \tilde{\xi} at \tilde{Y} = \tilde{h}(\tilde{t}) \\ \frac{\partial \tilde{U}}{\partial \tilde{Y}} = 0, \tilde{V} = 0, \frac{\partial \tilde{T}}{\partial \tilde{Y}} = 0, \frac{\partial \tilde{\Phi}}{\partial \tilde{Y}} = 0 \text{ at } \tilde{Y} = 0 \end{gathered} \tag{14}$$

3. SCALING ANALYSIS

Defining the following similarity transformations [43-45]:

$$\left.\begin{array}{l}\tilde{U}=\dfrac{a\tilde{X}}{2(1-a\tilde{t})}f^{'}(\eta),\tilde{V}=\dfrac{-a\tilde{H}}{2\sqrt{1-a\tilde{t}}}f(\eta),\\ \theta=\dfrac{\tilde{T}}{\tilde{T}_{\tilde{H}}},\Phi=\dfrac{\tilde{z}e\tilde{\Phi}}{k_B\tilde{T}_{\tilde{H}}},\eta=\dfrac{\tilde{Y}}{\tilde{H}\sqrt{1-a\tilde{t}}}.\end{array}\right\} \tag{15}$$

Introducing Eqn. (15) into the original momentum conservation Eqns. (2) and (3), the following non-dimensional momentum equations emerge:

$$\rho\left[\frac{a^2\tilde{X}}{4(1-a\tilde{t})^2}(2f^{'}(\eta)+\eta f^{''}(\eta)+(f^{'}(\eta))^2-f(\eta)f^{''}(\eta))\right]$$
$$=-\frac{\partial P}{\partial\tilde{X}}+\frac{\mu a\tilde{X}}{2\tilde{H}^2(1-a\tilde{t})^2}f^{'''}(\eta)-\frac{\sigma B^2 a\tilde{X}}{2(1-a\tilde{t})^2}f^{'}(\eta)+\frac{\tilde{\rho}_e E_X}{(1-a\tilde{t})}, \tag{16}$$

$$\rho\left[\frac{-a^2\tilde{H}}{4(1-a\tilde{t})^{3/2}}(f(\eta)+\eta f'(\eta)-f(\eta)f'(\eta))\right]=-\frac{\partial P}{\partial\tilde{Y}}-\frac{\mu a}{2\tilde{H}(1-a\tilde{t})^{3/2}}f''(\eta), \tag{17}$$

Converting PDEs of momentum equations into ODE to utilize transformation of similarities, so differentiating (16) w.r.t $\tilde{Y}$ and (17) w.r.t $\tilde{X}$ and subtracting both equations to eliminate the pressure gradient we proceed as follows.

$$\frac{\partial^2\tilde{P}}{\partial\tilde{X}\partial\tilde{Y}}=0 \tag{18}$$

Furthermore Eqn. (17) becomes:

$$f^{''''}(\eta)-S(3f^{''}(\eta)+\eta f^{'''}(\eta)-f(\eta)f^{'''}(\eta)+f^{''}(\eta)f^{'}(\eta))-Haf^{''}(\eta)+2U_e m^2\Phi^{'}=0 \tag{19}$$

The primitive energy conservation Eqn. (5) by virtue of Eqn. (15) assumes the dimensionless form:

$$\big(1+\varepsilon\theta(\eta)\big)\theta^{''}(\eta)+\varepsilon(\theta^{'}(\eta))^2-Pr\,S\,\theta^{'}(\eta)\big(\eta-f(\eta)\big)+$$
$$Pr\,E\,c((f^{''}(\eta))^2+4\delta^2(f^{'}(\eta))^2)+Ha^2Br\,f^{'2}(\eta)+\beta=0, \tag{20}$$

The zeta potential established throughout a large range of PH ionic solutions does not exceed 25 mV in all electric double layers. Therefore Eqn. (13) is linearized according to an estimate of a modest zeta potential and the resulting equation takes the form:

$$\Phi^{''}-m^2\sinh(\Phi)=0. \tag{21}$$

The associated dimensionless boundary conditions emerge as:

$$f(0) = 0, f''(0) = 0, \theta'(0) = 0, \Phi'(0) = 0, \\ f(1) = 1, f'(1) = 0, \theta(1) = 1, \Phi(1) = \xi. \Big\} \quad (22)$$

In Eqns. (19)-(21), $Pr = \frac{\mu c_p}{\bar{\kappa}}$is the Prandtl number, $S = \frac{a\rho\widetilde{H}^2}{2\mu}$is the Squeezing number, $Ha = \widetilde{H}B_0\sqrt{\frac{\sigma}{\mu}}$is the Hartmann (magnetic body force) number, $Ec = \frac{1}{\tilde{T}_{\widetilde{H}}c_p}\left(\frac{a\tilde{X}}{2(1-a\tilde{t})}\right)^2$is the Eckert (viscous heating) number, $\delta = \frac{\widetilde{H}\sqrt{1-a\tilde{t}}}{\tilde{X}}$is a dimensionless length, $\xi = \frac{\tilde{z}e\tilde{\xi}}{k_B\tilde{T}_{\widetilde{H}}}$is the zeta potential parameter, $Br = PrEc$ is the Brinkman number, $\beta = \frac{\sigma H^2 E_X^2}{\kappa T_H(1-a\tilde{t})}$, is the joule heating parameter, $U_e = \frac{1}{a\tilde{X}}U_{HS}$ is electric field parameter in which $U_{HS} = -\frac{k_B\tilde{T}_{\widetilde{H}}\varepsilon_{ef}E_X}{\mu\tilde{z}e}$ is the Helmholtz-Smoluchowski velocity, $m^2 = \kappa^2\widetilde{H}^2(1-a\tilde{t})$ is electroosmosis parameter where $\kappa^2 = -\frac{2\tilde{z}^2e^2\tilde{n}_0}{\varepsilon_{ef}k_B\tilde{T}_{\widetilde{H}}}$ is the Debye-Hückel parameter and $1/\kappa$is the Debye length which is also well-known as the characteristic thickness of the EDL.

3.1 Coefficient of skin friction

An important design parameter in tribology is the shear stress at the plate inner surfaces. The dimensional form of the coefficient of skin friction i. e. wall shear stress, can be defined as follows:

$$C_f = \frac{\mu}{\rho\nu^2}\left(\frac{\partial\widetilde{U}}{\partial\tilde{Y}}\right)_{\tilde{Y}=\tilde{h}(\tilde{t})}, \quad (23)$$

Using Eqn. (15) in Eqn. (23), we obtain the *dimensionless* skin friction coefficient as follows:

$$\frac{\widetilde{H}^2}{\tilde{X}^2}(1-a\tilde{t})R_{ex}C_f = f''(1). \quad (24)$$

Here $R_{ex} = \frac{2\rho\nu_H{}^2\tilde{X}\sqrt{1-a\tilde{t}}}{a\widetilde{H}\mu}$ is the local Reynolds number in which $\nu_H = -\frac{a\widetilde{H}}{2\sqrt{1-a\tilde{t}}}$, .

3.2 Nusselt number

The Nusselt number *Nu* provides quantification for the relative role of thermal convection to thermal conduction heat transfer modes. It also measures the heat transfer rate. At the upper plate surface, it may be defined as follows:

$$Nu = -\frac{H}{T_H}\left(\frac{\partial \tilde{T}}{\partial \tilde{Y}}\right)_{\tilde{Y}=\tilde{h}(\tilde{t})} \tag{25}$$

At the upper plate, the appropriate expression required is:

$$\sqrt{1-at}Nu = -\theta'(1). \tag{26}$$

4. Numerical Solution and Validation

The transformed, dimensionless nonlinear system of differential Eqns. (19)-(21), with boundary conditions i.e. Eqn. (22) has been solved with a shooting method in MATLAB software. This approach was effectively utilized in Zhang *et al*. [46]. The higher order differential Eqns. (19)-(21), are first converted into first-order equations:

$$\left.\begin{aligned} f_4{}' &= S(3f_3 + \eta f_4 - f_1 f_4 + f_3 f_2) + Ha^2 f_3 - 2U_e m^2 Z_2, \\ Y_2{}' &= \frac{-\varepsilon(Y_2)^2 + Pr\,S\,Y_2(\eta - f_1) - Pr\,E\,c((f_3)^2 + 4\delta^2(f_2)^2) - BrHa^2 f_2^2 - \beta}{(1+\varepsilon Y_1)}, \\ Z_2' &= m^2 Z_1. \end{aligned}\right\} \tag{27}$$

Where$f = f_1, f' = f_2, f'' = f_3, f''' = f_4, f^{iv} = f_4'$, $\Phi = Z_1, \Phi' = Z_2, \Phi'' = Z_2'$, $\theta = Y_1, \theta' = Y_2, \theta'' = Y_2'$.

According to the boundary conditions (21) and (22), the corresponding initial conditions are introduced as:

$$\left.\begin{aligned} &f_1(0) = 0, f_3(0) = 0, Y_2(0) = 0, Z_2(0) = 0, \\ &f_2(0) = a_1, f_4(0) = a_2, Y_1(0) = a_3, Z_1(0) = a_4. \end{aligned}\right\} \tag{28}$$

The values of a_1, a_2, a_3 and a_4 at the computation start point $\eta = 0$are assumed in order to integrate Eqn. (27) as a problem involving initial values. This is followed by the solution of the initial value problem (27)-(28) using a fourth-order Runge-Kutta algorithm. $\Delta\eta = 0.01$ value is selected for the step size. The boundary conditions (22) at $\eta = 1$ confirm the correctness of the anticipated values of a_1, a_2, a_3 and a_4. Due to high boundary residuals (10^{-10}), the starting values of a_1, a_2, a_3 and a_4 are calculated using a Newton-Raphson technique. After each iteration, the answer is evaluated to determine if it meets the required criterion. This concept is applied to create a programme with the help of MATLAB software. Validation of the MATLAB solutions for the current mathematical model is confirmed through the Table-1 for $f(\eta)$. Setting $U_e = 0, Ha = 0$ and with a fixed value of *S* = 0.05, the present model reduces exactly to the Newtonian squeezing flow model of Gupta and Gupta [47]. Very good agreement is achieved and consequently there is a high degree of confidence in MATLAB solutions. The residual error for various range of $10^{-3}, 10^{-6}$ and 10^{-9} versus axial velocity profile is clearly portrayed in **Fig. 2**. It is clearly observed that the error analysis is negligible form the computational point of view. Therefore, the entire graph is generated with a tolerance error of 10^{-9} which achieves highly accurate numerical results. The returned CUP time is calculated with the help of Matlab comment of *"cuptime"* from the proposed numerical solution. It is noted that the elapsed time is 1.000483 sec.

Table I. Comparison between the value of $f(\eta)$for the parallel plates from present numerical solution and from the work of Gupta and Gupta [47] with $Ha= U_e =0$ for *S* = 0.05.

η	Existing semi analytical results Gupta and Gupta [47]	Present numerical results	Absolute error
0.1	0.14996	0.149049881	0.00091
0.3	0.43766	0.435362187	0.002298
0.5	0.68881	0.686218942	0.002591
0.7	0.87934	0.877677595	0.001662
0.9	0.98565	0.985354894	0.000295

5. Numerical Results and Discussion

The main focus of this section is to investigate the MATLAB shooting numerical results which are all visualized in graphical form in **Figs. 3 – 15**. All data is extracted from reliable sources and provides a physically viable range of parameter values for the present simulations which are representative of actual electromagnetic lubrication squeezing systems- [9], [11], [15], [18], [24], [25]. [29] and [30]. This covers all physical effects featured in the current simulations i. e. electrical, magnetic, squeezing, thermal and hydrodynamic characteristics are properly represented with the data selected from these references. Numerical computations for velocity, fluid temperature, skin friction coefficient and Nusselt number for the influence of all key emerging parameters are examined. Both positive and negative values of electric field parameter U_e are considered. The electric field parameter$\left(U_e = \frac{1}{a\tilde{X}} U_{HS}\right)$ provides an important control mechanism for the squeezing flow. The electric field is the force that would experience the unit positive test charge when placed near the area around a charging system. The electrical field parameter value is negative when the electrical field is aligned in the positive axial direction (left to right in Fig. 1) but is positive when the axial electrical field is in the negative direction (right to left) i. e. when the direction of the electrical field is reversed. The electrical field direction therefore profoundly affects ion mobility in the squeezing parallel plate system. In terms of the squeeze number, the graphs consider two scenarios: when the plates are moving apart i. e. separating (S > 0) and when the plates are approaching i. e. squeezing (S < 0).

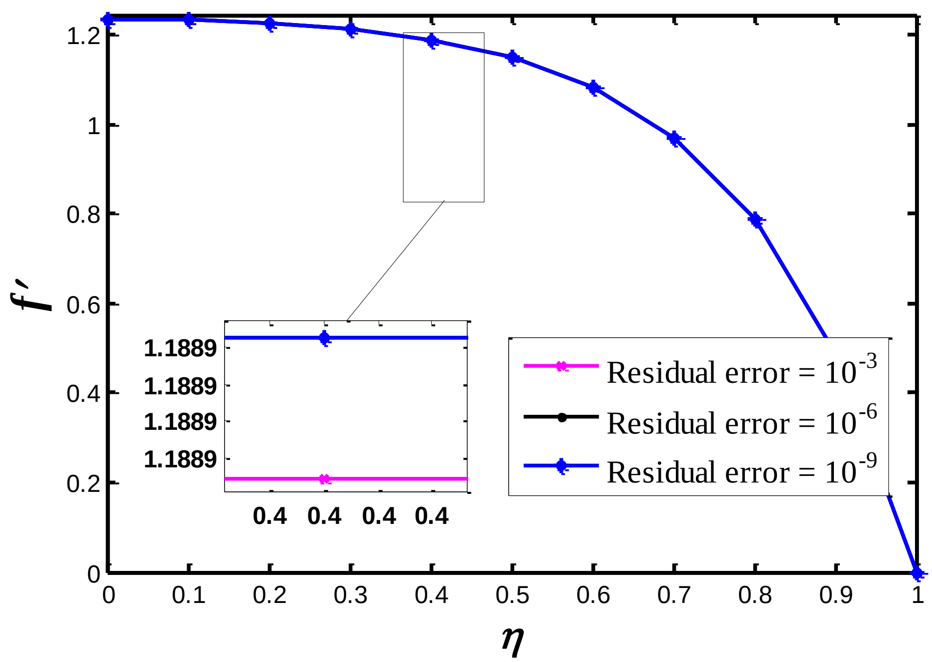

Fig. 2 Impact of residual error on $f'(\eta)$ when m = 1.5, S = 2, Pr = 2, Ec = 1, $\epsilon = 1,\ U_e = 1$ $\xi = 0.5$ and $Ha = 1$.

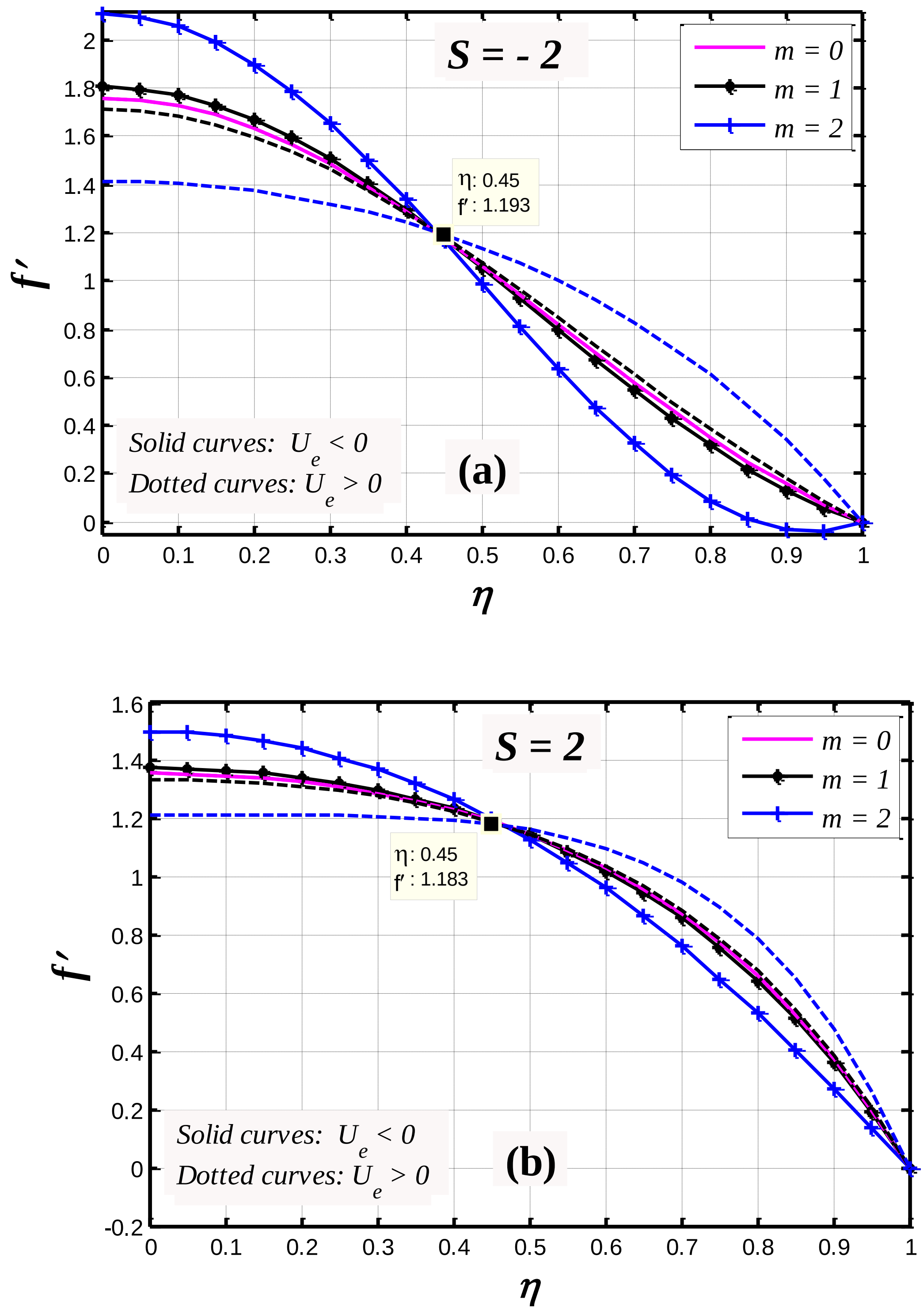

Fig. 3 Impact of m on $f'(\eta)$ for both $U_e < 0$ and $U_e > 0$

at (a) $S < 0$, (b) $S > 0$ when $\xi = 0.5$ and $Ha = 1$.

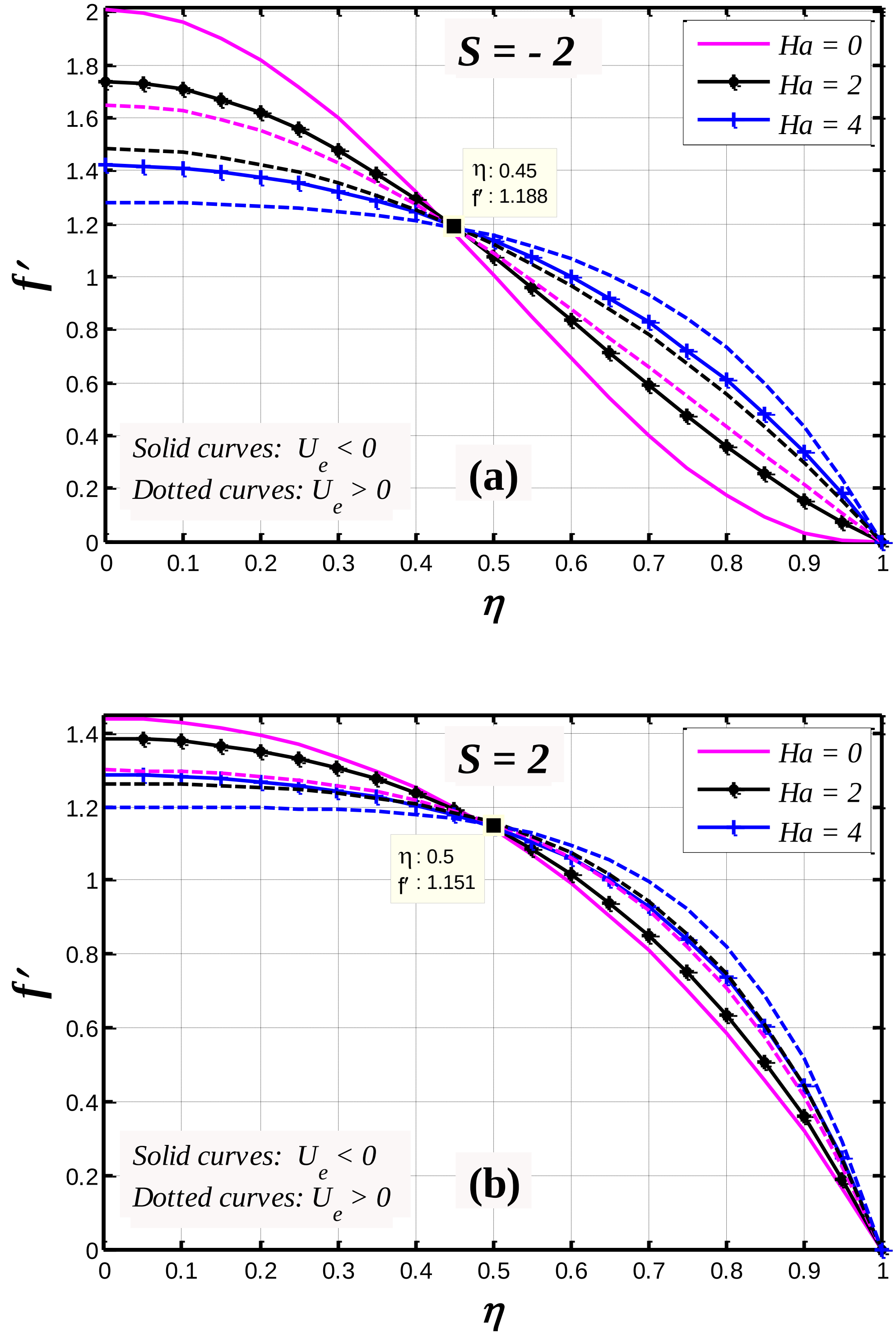

Fig. 4 Impact of Ha on $f'(\eta)$ for both $U_e < 0$ and $U_e > 0$

at (a) $S < 0$, (b) $S > 0$ when $\xi = 0.5$ and $m = 1.5$.

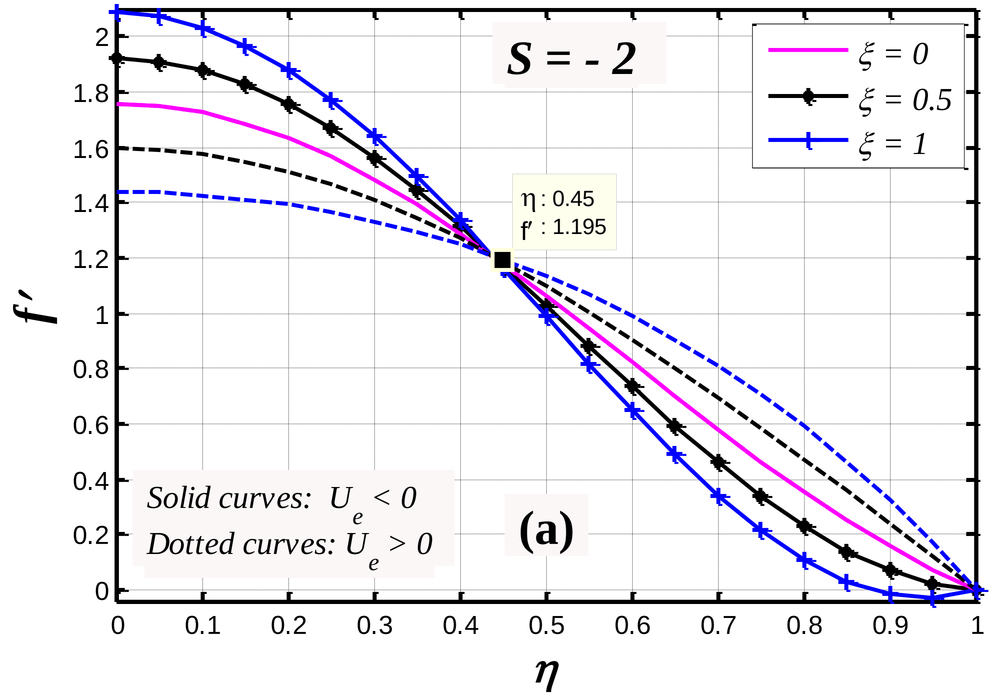

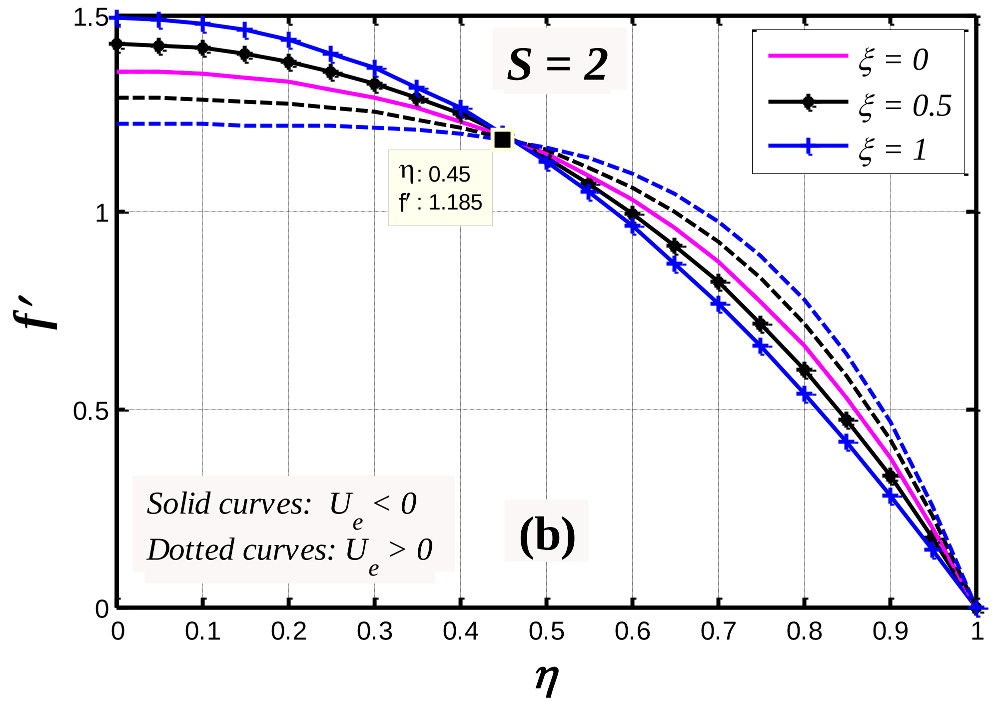

Fig. 5 Impact of ξ on $f'(\eta)$ for both $U_e < 0$ and $U_e > 0$

at (a) $S < 0$, (b) $S > 0$ when $m = 1.5$ and $Ha = 1$.

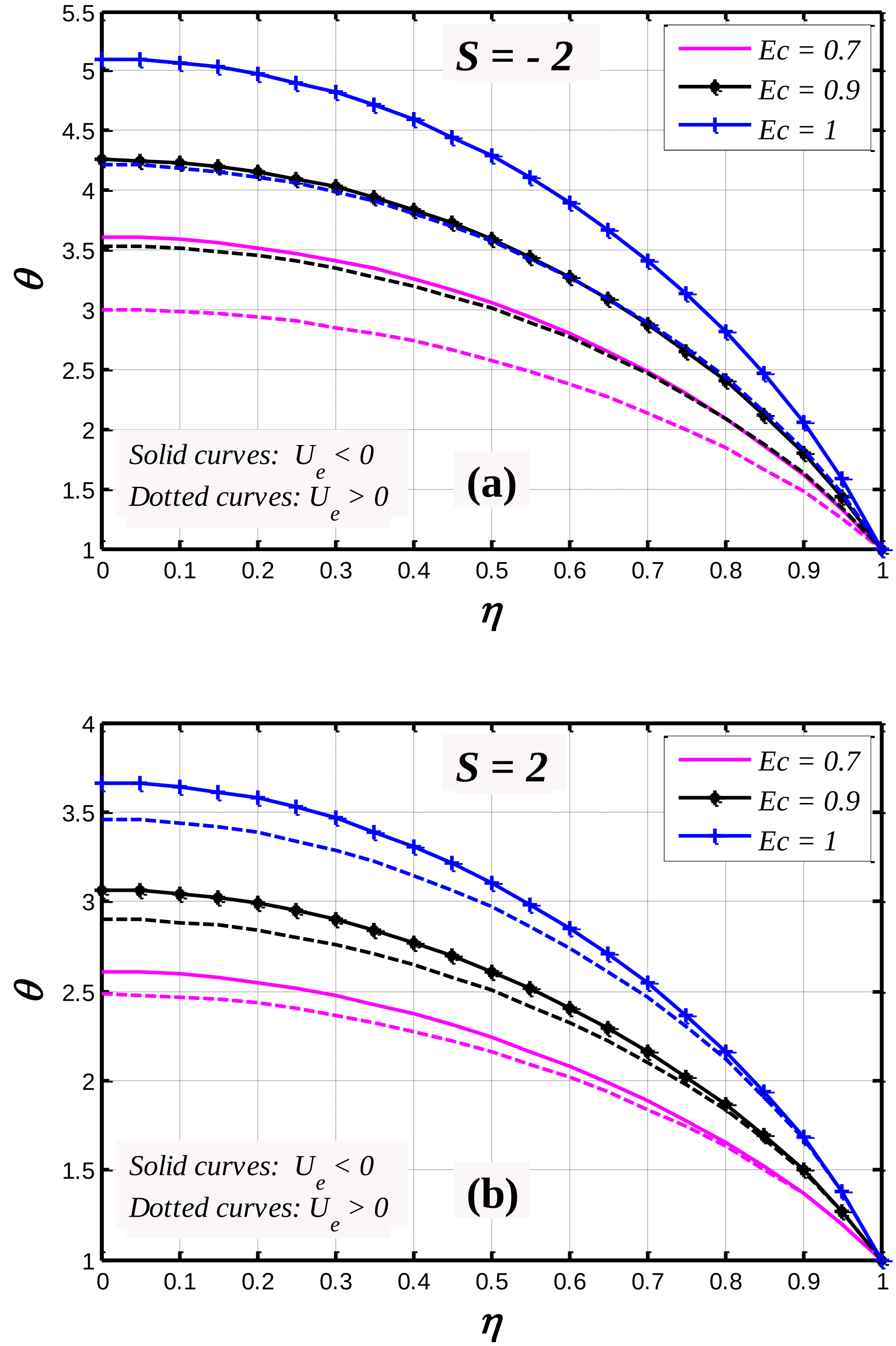

Fig. 6 Impact of Ec on $\theta(\eta)$ for both $U_e < 0$ and $U_e > 0$ at (a) $S < 0$, (b) $S > 0$ when $\xi = 0.5,\ m = 1.5, Pr = 1, \delta = 1, \beta = 0.5,\ \varepsilon = 1$ and $Ha = 1$.

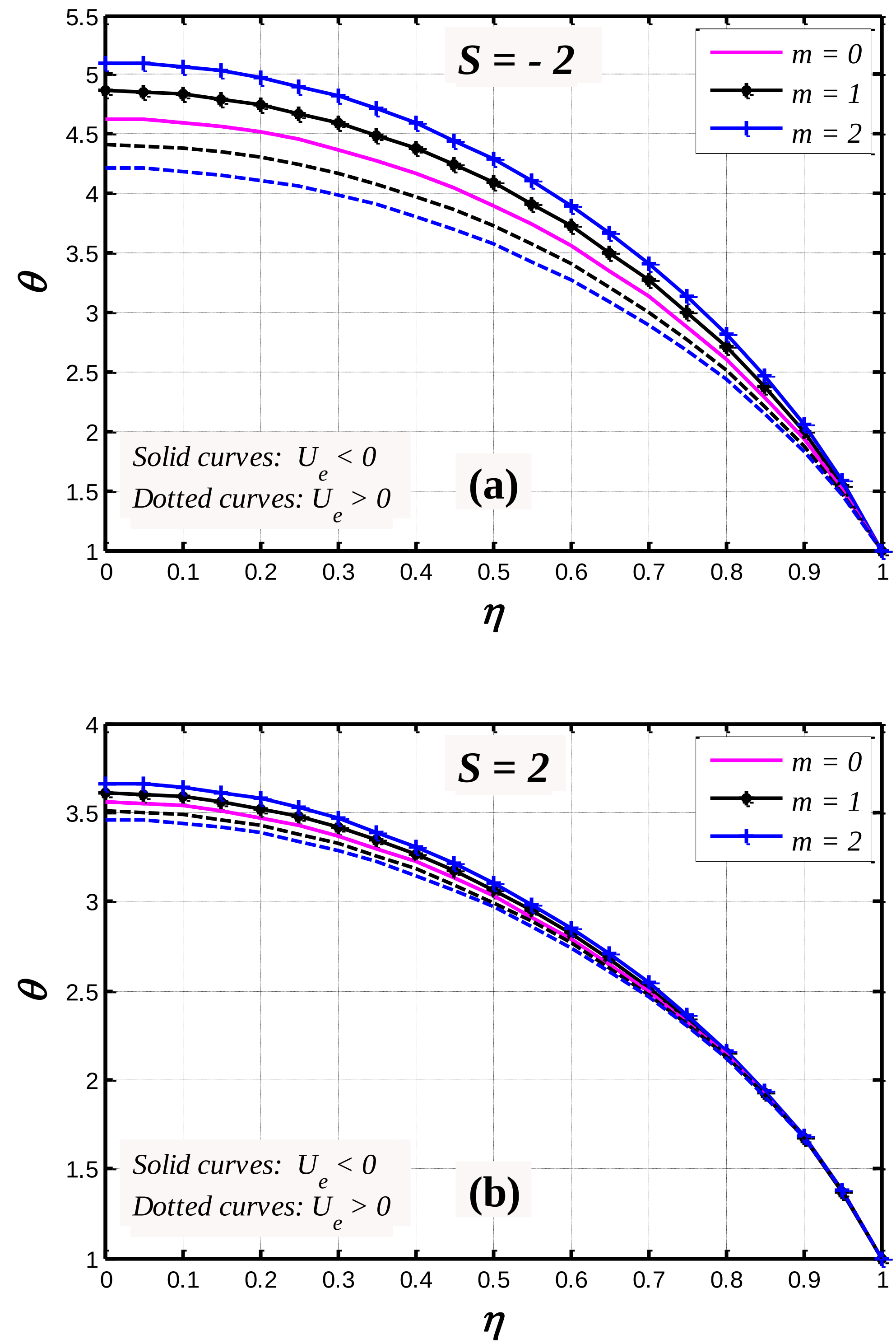

Fig. 7 Impact of m on $\theta(\eta)$ for both $U_e < 0$ and $U_e > 0$ at (a) $S < 0$, (b) $S > 0$ when $\xi = 0.5$, $Ec = 1$, $Pr = 2$, $\delta = 1$, $\beta = 0.5$, $\varepsilon = 1$ and $Ha = 1$.

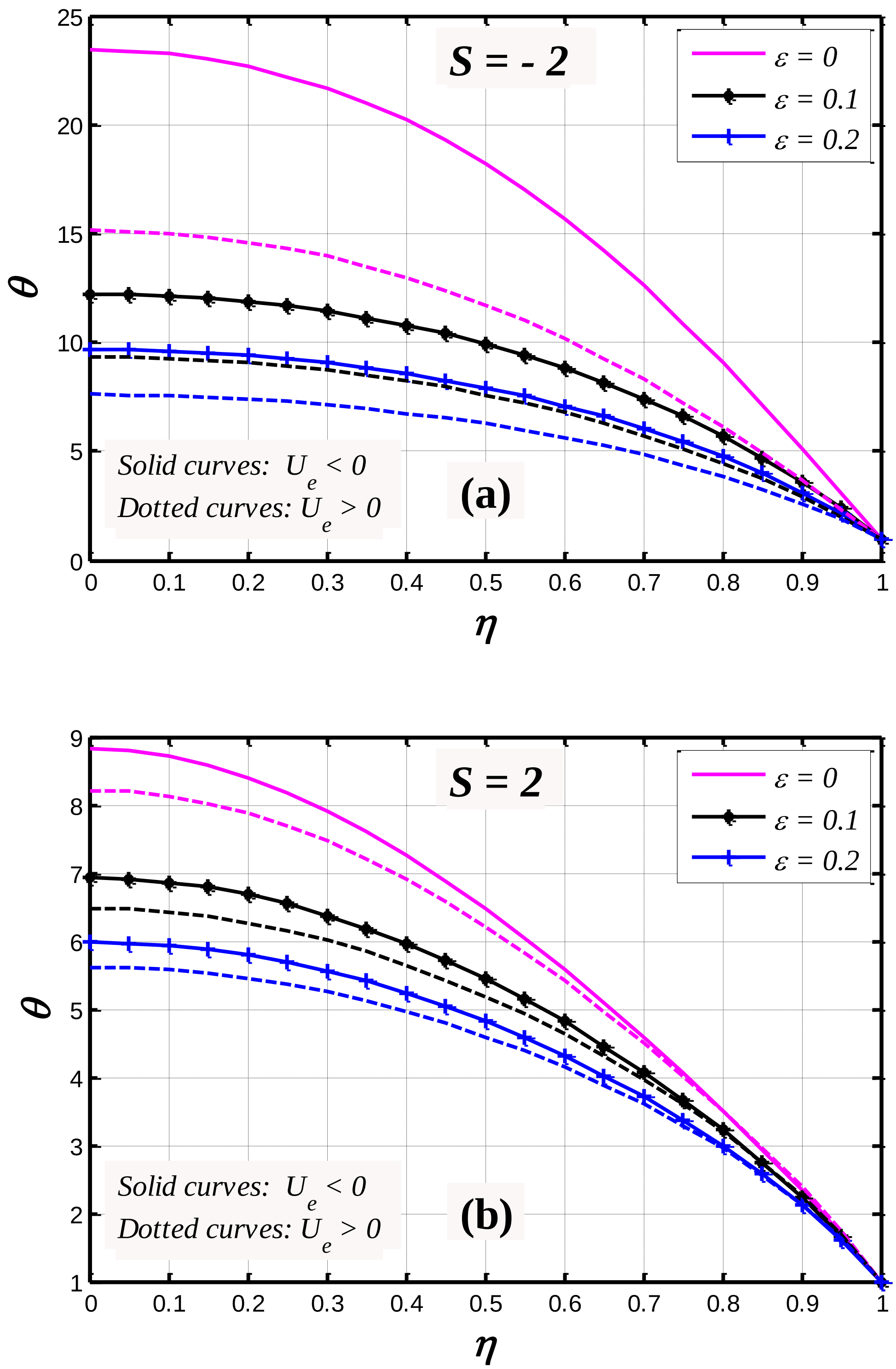

Fig. 8 Impact of ε on $\theta(\eta)$ for both $U_e < 0$ and $U_e > 0$ at (a) $S < 0$, (b) $S > 0$ when $\xi = 0.5$, $Ec = 1$, $Pr = 2$, $\delta = 1$, $\beta = 0.5$, $m = 1.5$ and $Ha = 1$.

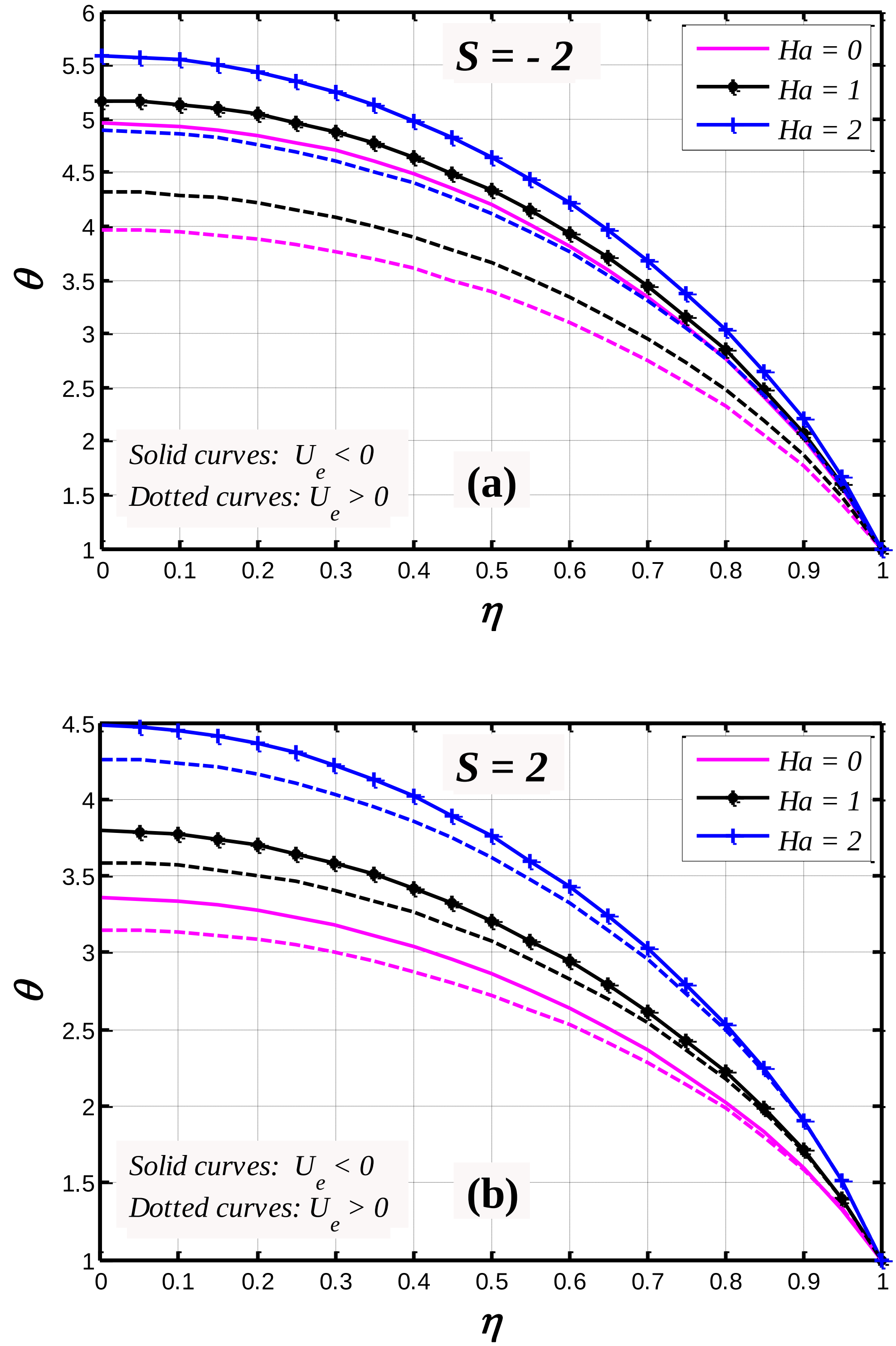

Fig. 9 Impact of Ha on $\theta(\eta)$ for both $U_e < 0$ and $U_e > 0$ at (a) $S < 0$, (b) $S > 0$ when $\xi = 0.5$, $Ec = 1$, $Pr = 2$, $\beta = 0.5$, $\delta = 1$, $m = 1.5$ and $\varepsilon = 1$.

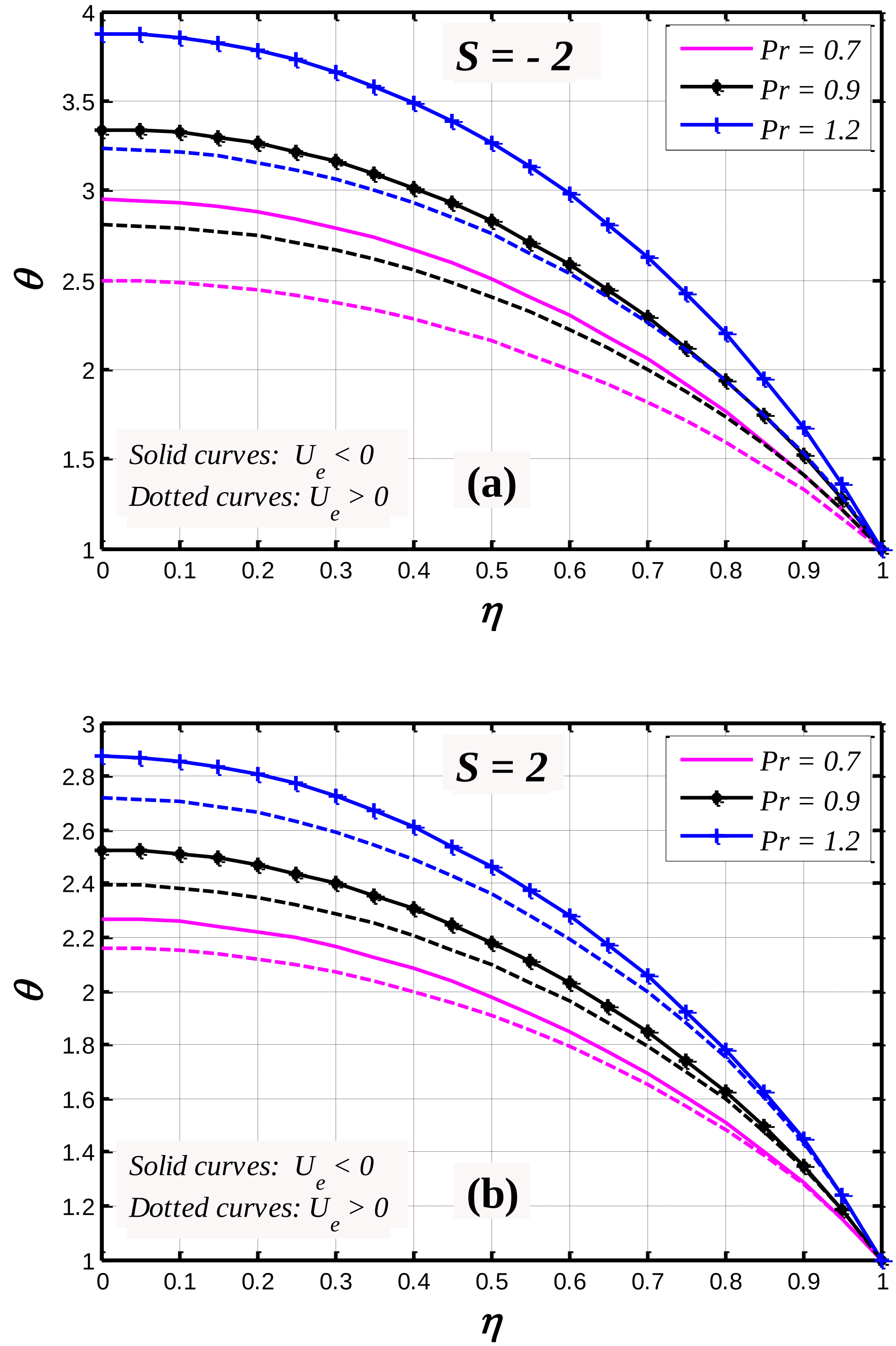

Fig. 10 Impact of Pr on $\theta(\eta)$ for both $U_e < 0$ and $U_e > 0$ at (a) $S < 0$, (b) $S > 0$ when $\xi = 0.5, Ec = 1, Ha = 1, \delta = 1, \beta = 0.5,\ m = 1.5$ and $\varepsilon = 1$.

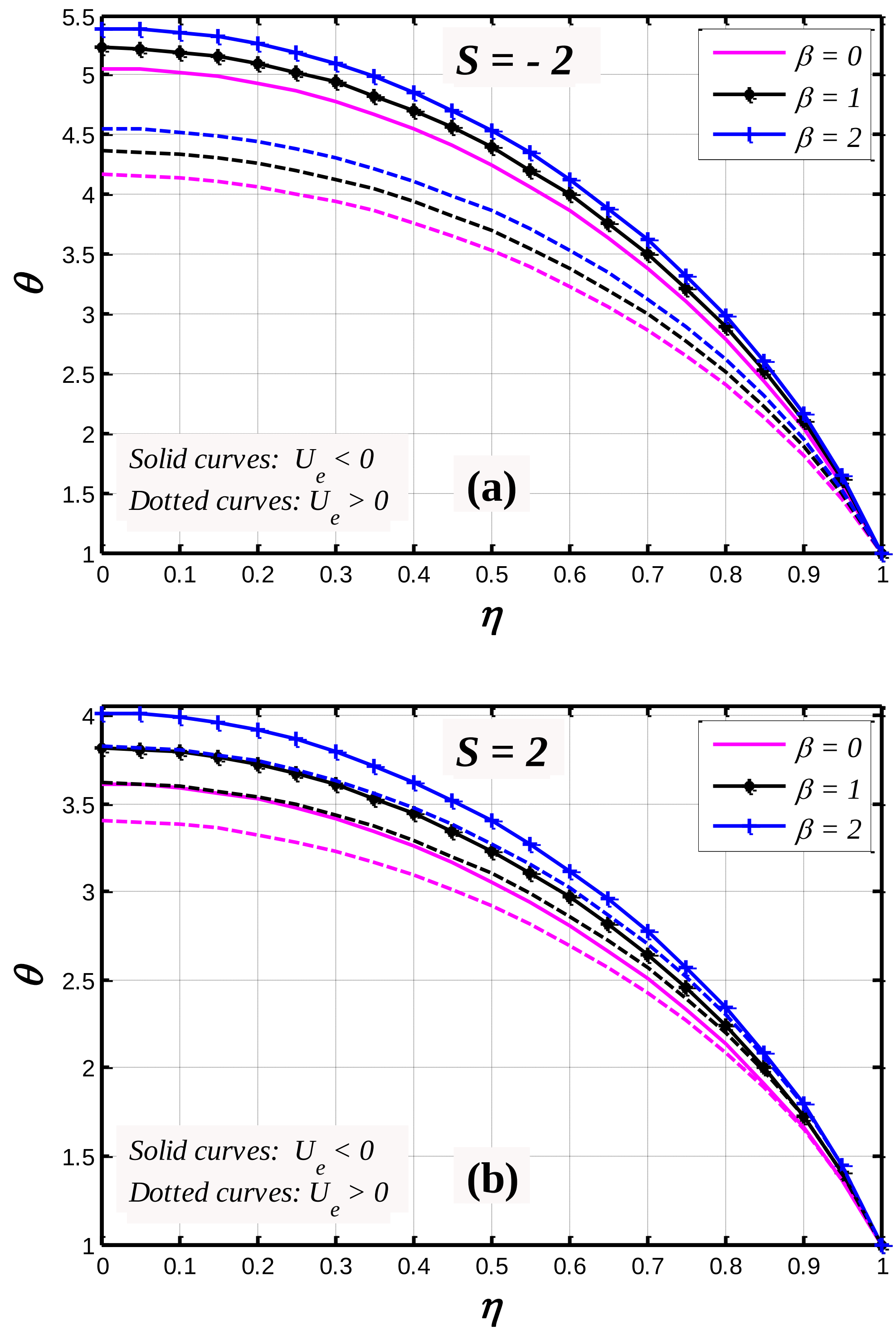

Fig. 11 Impact of β on $\theta(\eta)$ for both $U_e < 0$ and $U_e > 0$ at (a) $S < 0$, (b) $S > 0$ when $\xi = 0.5, Ec = 1, Ha = 1, \delta = 1, Pr = 2,\ m = 1.5$ and $\varepsilon = 1$.

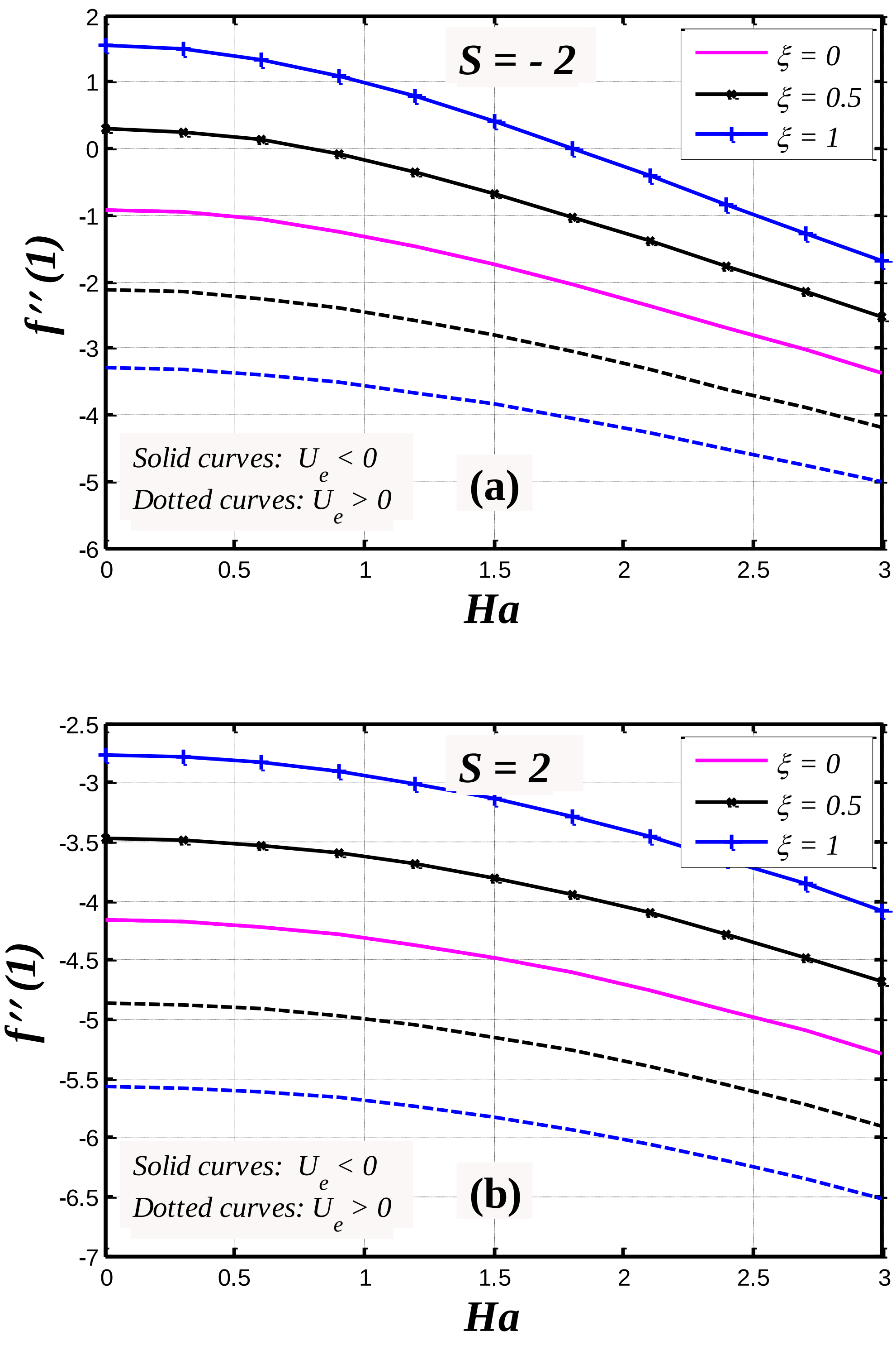

Fig. 12 Impact of ξ on $f''(1)$ for both $U_e < 0$ and $U_e > 0$

at (a) $S < 0$, (b) $S > 0$ when $m = 1.5$.

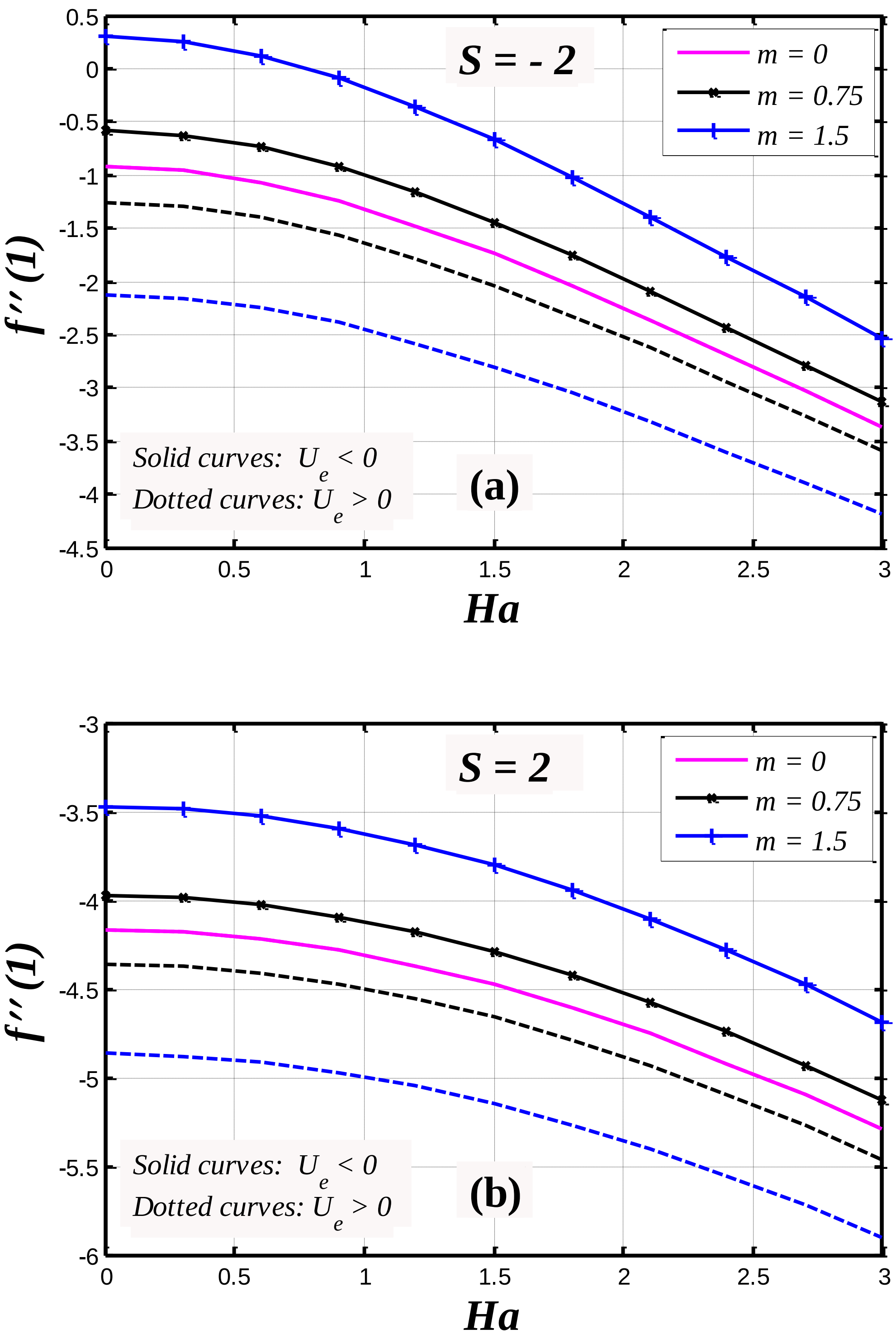

Fig. 13 Impact of m on $f''(1)$ for both $U_e < 0$ and $U_e > 0$

at (a) $S < 0$, (b) $S > 0$ when $\xi = 0.5$.

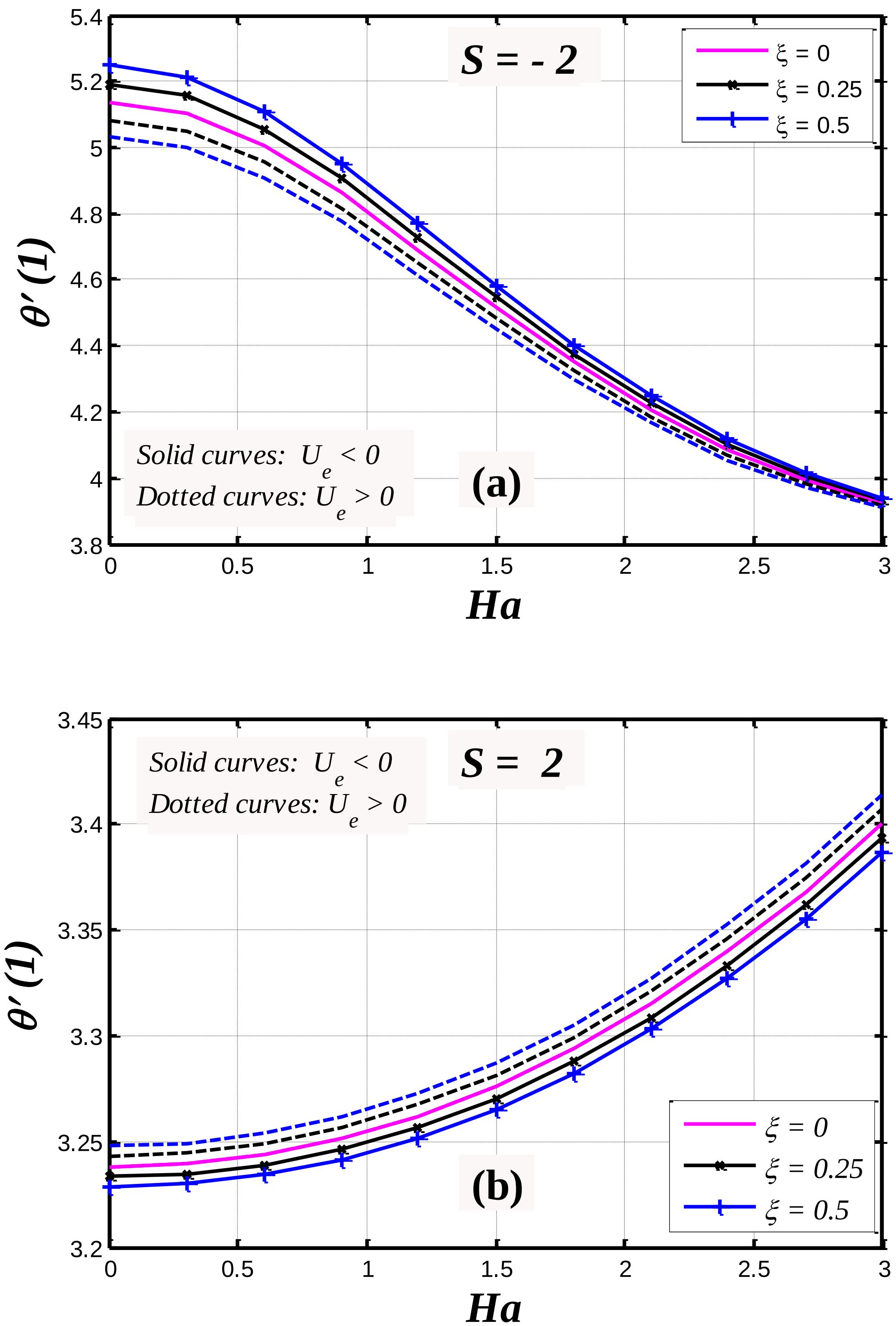

Fig. 14 Impact of ξ on $\theta'(1)$ for both $U_e < 0$ and $U_e > 0$ at (a) $S < 0$, (b) $S > 0$

when $Pr = 1, Ec = 0.5, \delta = 1, m = 1$ and $\varepsilon = 0.1$.

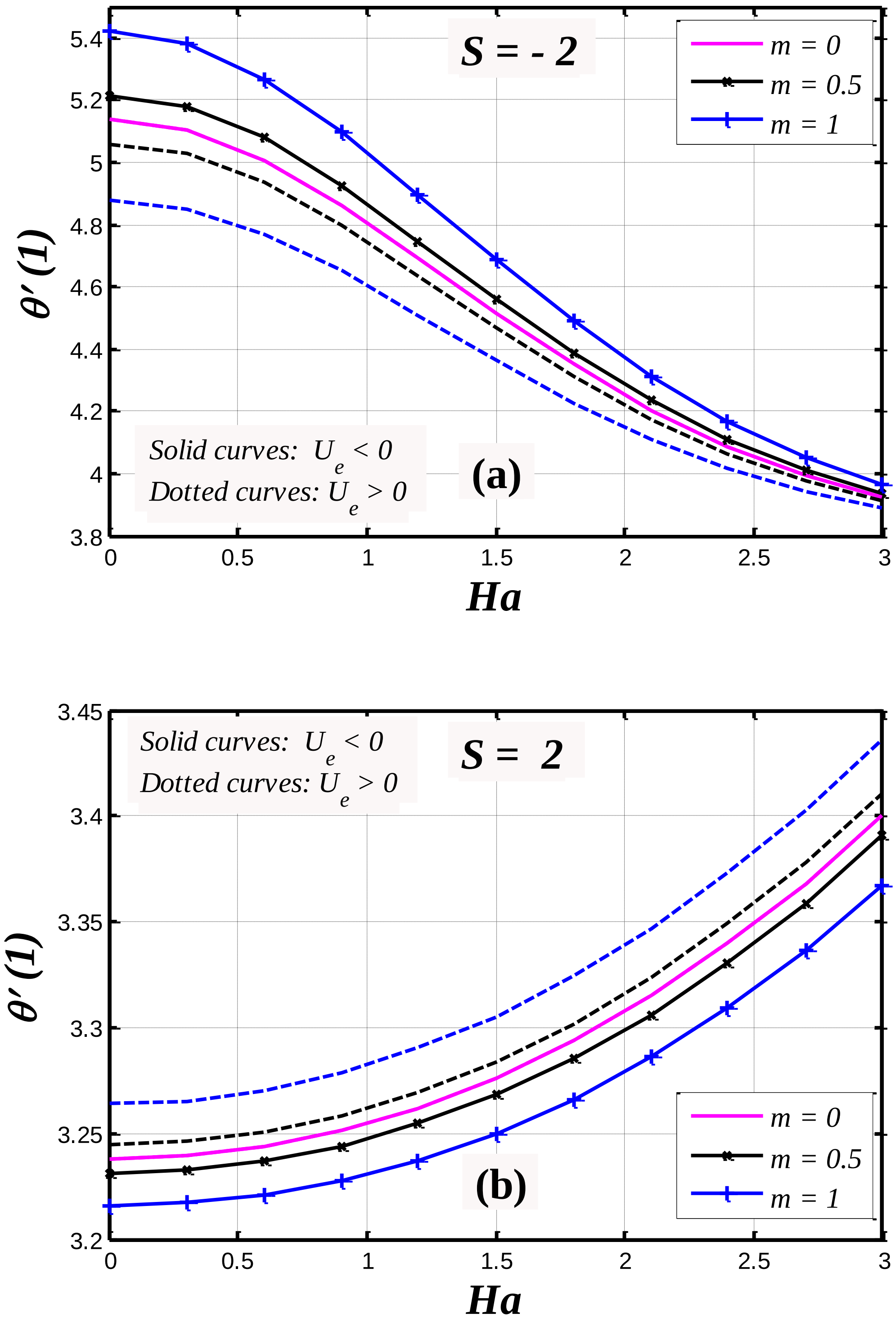

Fig. 15 Impact of m on $\theta'(1)$ for both $U_e < 0$ and $U_e > 0$ at (a) $S < 0$, (b) $S > 0$

when $Pr = 1, Ec = 0.5, \delta = 1, \xi = 0.5$ and $\varepsilon = 0.1$.

Figs. 3(a) – 3(b) show influence of electro osmosis parameter in the presence of negative and positive values of squeeze number (S) on fluid velocity for both $U_e < 0$ and $U_e > 0$. Fig. 3a corresponds to negative squeeze number, S = -2 i.e. squeezing. The behavior of axial velocity for both S < 0 and S > 0 are similar; however, magnitudes are greater for negative value of squeeze number compared with positive value of squeeze number near the lower plate. Also, higher magnitudes are computed for negative value of electric field parameter, $\left(U_e = \frac{1}{a\tilde{X}} U_{HS}\right)$ since for this case the axial electrical field assists the flow. If $U_e < 0$, the fluid velocity rises in the range of $0 \leq \eta < 0.45$ (approximately) and reduces in the range of $0.45 \leq \eta \leq 1$. This is attributable to intensification in collisions between particles near the parallel plates when the electroosmotic parameter (m) is raised. Therefore, the fluid velocity reduces close to the right boundary region and increases towards the left boundary. In the other case $U_e > 0$, the fluid velocity drops from $0 \leq \eta < 0.45$ and rises with in $0.45 \leq \eta \leq 1$. A similar trend is computed for positive value of squeeze number i. e. S = 2 (plates separating) in Fig. 3(b).

Figs. 4(a) – 4(b) portrays the impacts of Hartmann number with S < 0 and S > 0 on fluid velocity for both $U_e < 0$ and $U_e > 0$. The negative and positive value of squeeze numbers produce similar topologies of velocity distributions in the lower half space of the gap ($0 \leq \eta \leq 0.5$); however, in the upper half space of the gap ($0.5 \leq \eta \leq 1.0$) the velocity profiles for $Ha = 0$ are inverse parabolic for S = -2 (Fig. 4a) whereas they are *monotonic decays* for S = 2 (Fig. 4b). Increasing Hartmann number i. e. stronger magnetic field clearly damps the velocity in the lower half space whereas it induces acceleration in the upper half space, owing to momentum re-distribution. This effect is more pronounced for the plate squeezing case (Fig. 4a) compared with the plate separating case (Fig. 4b). Hartmann number expresses the relative contribution of magnetic (Lorentz) body force to the viscous hydrodynamic force. When Ha = 0, the magnetohydrodynamics effect is negated. When Ha = 1 both magnetic drag and viscous forces contribute equally, as noted by Cramer and Pai [48]. For Ha >1 the magnetic force exceeds the viscous force and this produces strong damping in the lower half space. Furthermore for $U_e < 0$ higher magnitudes are observed for velocity in the lower half space of the gap whereas for $U_e > 0$ greater magnitudes are computed in the upper half space. Evidently therefore assistive axial electrical field boosts momentum only in the lower half space of the gap whereas it inhibits momentum development and induces retardation in the upper half space. Clearly the combination of both transverse magnetic field and axial electrical field produces interesting behaviour in the squeezing flow regime. The associated parameters (*Ha*, U_e) can therefore be manipulated to produce acceleration/deceleration in the gap and also modify the pressure distribution which in turn will adjust the load carrying capacity of the system.

Figs. 5(a) – 5(b) visualize the impact of zeta potential parameter ξ for both squeezing i. e. $S < 0$ and separating i. e. $S > 0$ cases, again with both $U_e < 0$ and $U_e > 0$. The zeta potential parameter, $\xi = \frac{\tilde{z}e\tilde{\xi}}{k_B\tilde{T}_{\tilde{H}}}$arises in the upper plate boundary condition, $\Phi(1) = \xi$. With elevation in this parameter, there is a clear flow acceleration in the lower half space and deceleration in the upper half space. This is observed for both squeezing (Fig. 5a) and separating (Fig. 5b) cases. Electro-osmotic body force is generated when the electric field is applied to the magnetic ionic conductive solution (lubricant) with fixed charges on its interior wall. The negative ions (anions) are produced on the opposite plate surface which therefore has a net negative charge. This attracts positively charged cations from the bulk solution forming a double layer with positive charge density that decreases exponentially as the distance from the wall increases. The resulting potential difference very close to the wall is created and this is termed the zeta potential. An innermost layer close to the plate is essentially static and is termed the inner Helmholtz or Stern layer. In addition to this there will be a second layer which is more diffuse and is the outer Helmholtz plane (OHP). Under axial electrical field, the cations in the second more diffuse layer are mobilized towards the direction of the cathode (plate). This entrains solvent molecules in the magnetic ionic liquid and sustains the electroosmotic flow (EOF) between the plates. There is evidently, for U_e<0, flow acceleration in the lower half space i. e. approximately the region of $0 \leq \eta < (0.45, 0.45)$ whereas flow deceleration is produced in the upper half space of the regime i.e. $(0.45, 0.45) \leq \eta \leq 1$, as observed in (Fig. 5a). Zeta potential parameter therefore strongly modifies the velocity profiles throughout the gap region. The maximal fluid velocity is attained for negative value of electric field parameter and maximum zeta potential parameter at the lower plate (η=0) for the squeezing case (S< 0, Fig. 5a). Minimum fluid velocity is observed generally for positive electric field parameter at the upper plate (η=1) for both S < 0 (Fig. 5a) and S > 0 (Fig. 5b). The electrical potential variation across inner surfaces of the plates may also play an important role in mitigating corrosion and chemical surface degradation in tribological systems. For the case of $\xi = 0$, velocity is minimized in the lower half space whereas it is maximized in the upper half space, for both squeezing (Fig. 5a) or separating plate (Fig. 5b) cases. It is also interesting to note that the electro-osmotic flow mobilizing transport produces *warped parabolic profiles* across the channel, distinct to the *classical parabolic profiles* associated when only pressure is used to pump lubricant in conventional non-electrical systems.

Figs. 6(a) – 6(b) visualize the impact of Eckert number on temperatures again for both S < 0 (Fig 6a) and S > 0 (Fig. 6b), also for both $U_e < 0$ and $U_e > 0$. *Ec* arises only in the viscous heating term in the transformed energy Eqn. (21), viz $+ Pr\, E\, c((f''(\eta))^2)$. It embodies the ratio of kinetic energy dissipated to the enthalpy difference (product of temperature difference and specific heat capacity i.e. $\tilde{T}_{\tilde{H}} c_p$) across the gap. A significant boost in temperature is therefore computed from the lower plate to the upper plate, although there is a sustained monotonic decay in temperatures across the gap. Maximum temperature is therefore computed consistently at the lower plate and vice versa at the upper plate, in both Figs 6a and b. Generally higher temperatures with $U_e < 0$. However, for the squeezing case (S < 0, Fig. 6a) temperature magnitudes are significantly higher, especially at the lower plate.

Figs. 7(a) – 7(b) display the impact of electroosmosis parameter (m) on temperature profiles in the gap, again for both negative and positive squeeze number, also for the two cases of $U_e < 0$ and $U_e > 0$. It is evident from both Fig. 7(a) and 7(b), that there is a significant elevation in the fluid temperature with increasing m values. Hence an increment in the length of Debye parameter for negative electric field parameter, generally boosts temperatures. Higher values of temperature are achieved with $U_e < 0$ compared with $U_e > 0$.The electroosmosis parameter,$m^2 = \kappa^2 \tilde{H}^2 (1 - a\tilde{t})$ where $\kappa^2 = -\frac{2\tilde{z}^2 e^2 \tilde{n}_0}{\varepsilon k_B \tilde{T}_{\tilde{H}}}$ is the Debye-Hückel parameter and $\frac{1}{\kappa}$ is the Debye length (characteristic thickness of the EDL). Since the Debye length parameter m and the electric double layer (λ_d) thickness of $m \propto \kappa$ for a given kinematic viscosity, and gap distance $\tilde{h}(t)$, a thinner EDL will be generated in the regime, for both S < 0 and S > 0. The electric potential enhances mobility of ion transport. This encourages thermal diffusion in the regime and elevates temperatures, although as noted higher temperatures are produced for $U_e < 0$ compared with $U_e > 0$. Generally, temperatures are minimized for the case m = 0, for which the electro-osmotic effect is negated. Again, significantly higher temperatures are computed for the squeezing case (Fig. 7a, S=-2) relative to the plate separating case (Fig. 7b, S= 2).

Figs.8(a)-(b) illustrate the influence of thermal conductivity parameter (ε) on temperatures for both $S < 0$, $S > 0$ and the two cases of $U_e < 0$ and $U_e > 0$. The thermal conductivity variable parameter is expressed as a temperature-dependent linear function and features in multiple terms in the energy Eqn. (20) i.e. $\big(1 + \varepsilon\theta(\eta)\big)\theta''(\eta)$, $\varepsilon(\theta'(\eta))^2$. The thermal diffusion terms are therefore strongly modified by this parameter. As ε is increased from 0, through 0.25 to a maximum of 0.5, thermal conductivity of the magnetic ionic lubricant is reduced, and there is a marked depletion in temperatures across the gap, for both squeezing (Fig. 8a) and plate separating (Fig. 8b) scenarios. As a result, heat diffuses more slowly in the gap for $\varepsilon > 0$, compared with ε =0 for which thermal conductivity is highest. Again, much higher temperatures are again computed for the squeezing scenario (Fig 8a, S = -2) compared with the plate separating case (Fig. 8b, S = 2). Furthermore for $U_e < 0$ temperature magnitudes are again higher than they are for $U_e > 0$. This effect is maximized at the lower plate and progressively diminishes across the gap to the upper plate.

Figs.9(a)-9(b) visualizes the evolution in temperature across the gap with variation in Hartmann number (Ha) again for both $S < 0$ and $S > 0$ for both $U_e < 0$ and $U_e > 0$. It is noticed that the fluid temperature distribution increase from the lower plate to the upper plate surface when Hartmann number is increased for both $U_e < 0$ and $U_e > 0$. In the absence of Hartmann number (absence of transverse magnetic field), minimum temperatures are computed for both negative (Fig. 9a) and positive (Fig. 9b) squeeze numbers. The influence of magnetic field therefore is distinct from classical magnetohydrodynamics where temperatures are usually elevated due to work expended in dragging the fluid against the Lorentz body force and this supplementary work is expended as thermal energy. In the present magnetic ionic squeezing regime, the opposite effect is produced and this is probably attributable to the inclusion of axial electrical field which also modifies the influence of magnetic field on the regime.

Figs. 10(a) – 10(b) indicates the influence of Prandtl number for both $S < 0$ and $S > 0$ on the fluid temperature and again for both cases of $U_e < 0$ and $U_e > 0$. Temperatures are elevated with rising values of the Prandtl number for both case of $U_e < 0$ and $U_e > 0$. Prandtl (Pr) number relates the relative rate of diffusion of momentum to energy in the magnetic ionic lubricant. When Pr is small, ($Pr < 1$), this indicates that thermal diffusivity is dominant over momentum diffusivity. When Pr > 1 momentum diffusivity takes precedence over thermal diffusivity. Higher temperatures are observed for the squeezing case (Fig. 10a) than the plate separating case (Fig. 10b). Also, once for $U_e < 0$ temperatures computed are significantly greater than for $U_e > 0$. Strong monotonic decays are observed in both Fig. 10a, b with maximum temperature computed always at the lower plate and minimal temperatures at the upper plate, irrespective of the Prandtl number prescribed.

Figs. 11(a) – 11(b) depict temperature profiles for various values of the Joule heating parameter with fixed values of other parameters for both $S < 0$, $S > 0$ and the two cases of $U_e < 0$ and $U_e > 0$.When the axial electrical field is applied in a capillary to create electroosmotic flow, it is noticed that the electric current travelling through the buffer solution results in Joule heating. After passing through the capillary parallel plate, the Joule heat is released into the surrounding environment without being constrained by convection. The temperature magnitudes found for the case of negative Helmholtz Smoluchowski velocity are much larger than those obtained for the case of positive Helmholtz Smoluchowski velocity over the same increase in Joule heating parameter, as has been shown for both $S < 0$ and $S > 0$.

Figs. 12(a) – 12(b) depicts the influence of zeta potential (ξ) on skin friction coefficient, $f''(1)$ at the upper plate versus Hartmann number (*Ha*), again for the two cases of $U_e < 0$and $U_e > 0$. In both plots there is a clear decay in skin friction at the upper plate with increment in Hartmann number. Increasing transverse magnetic field clearly depletes skin friction since the Lorentz body force retards the flow between the gap. Conversely increasing zeta potential (ξ) enhances the skin friction coefficient, $f''(1)$ *i.e. induces acceleration at the upper plate* for $U_e < 0$ whereas it is reduces skin friction for $U_e > 0$. *This difference in response is again associated with the direction of the applied electrical field.* Similar trends are observed for both the squeezing case (Fig 12a, $S = -2$) and the plate separating case (Fig. 12b, $S = 2$). However, in the squeezing case (Fig. 12a), strong back flow (negative skin friction) is computed for $U_e > 0$ whereas in the separating plate case (Fig. 12b) flow reversal is apparent for both cases of $U_e < 0$and $U_e > 0$, across the entire gap. In practical designs, therefore the squeezing case generally is more advisable since backflow can be eliminated for $U_e < 0$ at least in the lower half space of the gap. A judicious selection of magnetic field (Hartmann number) and zeta potential (ξ) therefore can enable either strong flow deceleration or flow acceleration to be generated in the regime. Furthermore, these mechanisms can be employed to charge stability of the magnetic ionic lubricant dispersed system.

Figs. 13(a)-13(b) depicts the influence of electro-osmotic parameter (*m*), on skin friction coefficient, *f*$^{//}$*(1)* at the upper plate versus Hartmann number (*Ha*), again for the two cases of $U_e <$ 0and $U_e > 0$. As with Figs. 13a, b, there is significant depletion in skin friction with increment in Hartmann number, for both squeezing (Fig. 13a) and plate separating (Fig. 13b) cases. With increment in m values however the skin friction is enhanced for $U_e < 0$ whereas it is reduced for $U_e > 0$. In other words, once again, the orientation of the axial electrical field has a profound influence on the skin friction. Assistive electrical field (reverse direction) accelerates the flow whereas inhibiting electrical field (positive axial direction) produces flow retardation. Again, *reverse flow is present always* on the upper disk for the plate separating case (Fig. 13b) whereas there is a small range for which it is eliminated for the squeezing case (Fig. 13a- top corner of the plot).

Figs. 14(a)-(b) illustrate the numerical results of Nusselt number function, $\theta'(1)$, versus Hartmann number (*Ha*) and electrokinetic zeta potential parameter (ξ)) , for both squeezing, S < 0 and separating plates, S > 0 and again with $U_e < 0$and $U_e > 0$. Heat transfer rate (Nusselt number) at the upper plate is clearly suppressed with increasing Hartmann number for the squeezing case (Fig 14a) whereas it is significantly enhanced for the plate separating case (Fig. 14b). The proximity of the plates there has a profound effect on magnetic field influence on the heat transfer to the upper plate. For the *squeezing* case (Fig. 14a), increasing electrokinetic zeta potential parameter (ξ) is observed to elevate Nusselt number function, $\theta'(1)$ for $U_e < 0$. The converse response is however computed for $U_e > 0$ i. e. $\theta'(1)$ magnitudes are suppressed with increasing zeta potential parameter (ξ). The implication is that the combination of direction of axial electrical field and transverse magnetic field induce different thermal behaviors in the system. For the *plate separating* case (Fig. 14b), the opposite trends are observed. For increment in electrokinetic zeta potential parameter (ξ), Nusselt number function, $\theta'(1)$ for $U_e > 0$ whereas it is depleted for $U_e < 0$.

Figs. 15(a)-(b) present the evolution in Nusselt number function, $\theta'(1)$, versus Hartmann number (*Ha*) and electro-osmotic parameter (*m*), for both squeezing, S < 0 and separating plates, S > 0 and again with $U_e < 0$and $U_e > 0$. Similar behavior is noted for increment in Hartmann number, as in Figs. 15(a)-(b) i. e. $\theta'(1)$ magnitudes are boosted for the squeezing case (Fig. 15a) but suppressed for the plate separating case (Fig. 14b). With increasing *m* values, Nusselt number function is *enhanced* for $U_e < 0$ but *reduced* for $U_e > 0$ in the squeezing case (Fig. 15a) i. e. for

S = -2. However, in the plate separating case (Fig. 15b) i. e. for S = 2, Nusselt number magnitudes are depressed for $U_e < 0$ whereas they are increased for $U_e > 0$, with increment in the electro-osmotic parameter (m)). Overall, significantly higher magnitudes of Nusselt number function, $\theta'(1)$ are produced for any Hartmann number (Ha) for the squeezing, S < 0 case (Fig. 15a) relative to the separating plate case, S > 0 (Fig. 15b). This emphasizes the earlier observation that there exists a complex interplay between electrical body force, Lorentz magnetic body force and also the state of the parallel plates, all of which must be carefully selected to achieve the desired heat transfer behavior and optimum lubrication performance.

6. Conclusions

Inspired by hybrid electro-magnetic ionic smart lubrication systems, in this work a novel mathematical model has been developed for unsteady electro-magnetohydrodynamics (EMHD) squeezing flow and heat transfer in a smart ionic viscous fluid with zeta potential effects between parallel plates. Viscous dissipation and variable thermal conductivity effects are included. The governing equations are converted into ordinary differential equation by using similarity transformations and then solved numerically subject to appropriate boundary conditions at both lower and upper plates, with MATLAB software. Validation with simpler non-magnetic and non-electrical squeezing flow solutions from the literature is included. A parametric study of the impact of squeezing number, variable thermal conductivity parameter, Prandtl number, Hartmann number, Eckert number, zeta potential parameter, electric field parameter and electroosmosis parameter on the axial velocity, fluid temperature and upper plate Nusselt number is conducted. The main findings of the present simulations may be summarized as follows:

a) Axial velocity acceleration is induced with negative squeeze number (plates approaching, S< 0) in comparison to that of positive squeeze number (plates separating, S>0).
b) Velocity is boosted with increasing electroosmosis parameter and zeta potential parameter.
c) Nusselt number is reduced with greater thermal conductivity parameter.
d) With rising values of zeta potential and electroosmosis parameter, there is a decrease in temperatures for $U_e > 0$ for both approaching i. e. squeezing plates (S < 0) and separating (S >0) cases.
e) With increment in Hartmann number, Nusselt number magnitudes are boosted for the squeezing case but suppressed for the plate separating case.

f) Increasing zeta potential (ξ) enhances the skin friction coefficient, $f^{//}(1)$ *i.e. induces acceleration at the upper plate* for $U_e < 0$ whereas it is reduces skin friction for $U_e > 0$.

g) The direction of the applied axial electrical field (assistive or inhibiting) in combination with the transverse magnetic field and plate squeezing/separating, significantly modifies the thermo-fluid characteristics in the magnetic ionic lubrication regime.

h) Increasing Joule parameter accelerates the fluid temperature flow for both for both squeezing, $S < 0$ and separating plates, $S > 0$ and again with $U_e < 0$ and $U_e > 0$ in the parallel plates.

The present analysis has revealed some interesting features of electro-magnetic ionic squeeze film tribology. However Newtonian behaviour has only been considered. Future investigations may address non-Newtonian (e. g. power-law [49] or viscoplastic, viscoelastic, microstructural etc.) characteristic. Additionally, alternative semi-numerical/analytical methods may be deployed in future investigations including the Differential transform method [50] and homotopy analysis method [51-52] to compute power series solutions. Efforts in this regard will be communicated imminently.

References

1. Jackson, J. D. A study of squeezing flow. *Applied Scientific Research, Section A* 11, no. 1 (1963): 148-152.
2. Singh, P., V. Radhakrishnan, and K. A. Narayan. Squeezing flow between parallel plates. *Ingenieur-Archiv* 60, 4 (1990): 274-281.
3. Ghori, Q. K., M. Ahmed, and A. M. Siddiqui. Application of homotopy perturbation method to squeezing flow of a Newtonian fluid. *International Journal of Nonlinear Sciences and Numerical Simulation* 8, no. 2 (2007): 179-184.
4. Wilson, S. D. R. Squeezing flow of a Bingham material. *Journal of Non-Newtonian Fluid Mechanics* 47 (1993): 211-219.
5. Campanella, Osvaldo H., and Micha Peleg. Squeezing flow viscometry for nonelastic semiliquid foods—theory and applications. *Critical Reviews in Food Science and Nutrition* 42, no. 3 (2002): 241-264.
6. B. Bushan, *Introduction to Tribology*, Second Edition, John Wiley, USA (2013).

7. E. Chandrasekharan and G. Ramanaiah, Unsteady flow between rectangular plates and between circular plates, *Wear*, 91, 307-318 (1983).
8. R. C. Bhattacharjee and N. C. Das, Analysis of an unsteady squeezing flow of dusty fluids, *Tribology International*, 32, 427-434 (1999).
9. W.F. Hughes, Magnetohydrodynamic lubrication and application to liquid metals, *Industrial Lubrication and Tribology*, Vol. 15 No. 3, pp. 125-133 (1963).
10. J. Jia *et al.,* Effects of magnetic ionic liquid as a lubricant on the friction and wear behavior of a steel-steel sliding contact under elevated temperatures, *Friction, 9,* 61–74 (2021).
11. J. Krim, Controlling friction with external electric or magnetic fields: 25 examples**,** *Front. Mech. Eng*., 21, 1-28 (2019).
12. Wang Z Z, Li D C, Zhou J. Non-uniform distribution of magnetic fluid in multistage magnetic fluid seals. *J Magn.,* **22** (2): 299–305 (2017).
13. L. Xu *et al.,* A novel compound mechanical seal of reusable rocket turbopump with superconducting magnetic force improving lubrication and stability, *Tribology International*, 159, 106989 (2021).
14. N.B.Naduvinamani *et al.,* Combined effects of MHD and surface roughness on couple-stress squeeze film lubrication between porous circular stepped plates, *Tribology International, 56*, 19-29 (2012).
15. J.C. Umavathi, S.L. Patil, B. Mahanthesh and O. Anwar Bég, Unsteady squeezing flow of magnetized nano-lubricant between parallel disks with Robin boundary condition, *Proc. IMechE J. Nanomaterials, Nanoengineering and Nanosystems (2021). DOI: 10.1177/23977914211036562 (15 pages)*
16. L.M. Chu *et al*., Pure squeeze motion in a magneto-elastohydrodynamic lubricated spherical conjunction, *ASME J. Tribology*, 132(4): 044501 (2010).
17. Shah RC, Shah RB. Ferrofluid lubrication of circular squeeze film bearings controlled by variable magnetic field with rotations of the discs, porosity and slip velocity. *R. Soc. Open Sci.* 4: 170254 (2017).
18. Prajapati BL. Magnetic-fluid-based porous squeeze films, *J. Magn. Magn. Mater.* **149**, 97–100 (1995).

19. Khan, Umar, Naveed Ahmed, Z. A. Zaidi, Mir Asadullah, and Syed Tauseef Mohyud-Din. MHD squeezing flow between two infinite plates. *Ain Shams Engineering Journal,* 5, 1 187-192 (2014).
20. İ. Çelika *et al.,* Heat Transfer and velocity in the squeezing flow between two parallel disks by Gegenbauer Wavelet Collocation Method, *Proceedings of 5th International Conference on Modern Approaches in Science, Technology & Engineering STECONF, 29-31 August, Berlin, Germany* (2019).
21. Hayat, T., M. Waleed Ahmed Khan, A. Alsaedi, and M. Ijaz Khan. Squeezing flow of second grade liquid subject to non-Fourier heat flux and heat generation/absorption. *Colloid and Polymer Science* 295, no. 6 (2017): 967-975.
22. M. Shamshuddin, S.R. Mishra, Ali Kadir and O. Anwar Bég, Unsteady chemo-tribological squeezing flow of magnetized bioconvection lubricants: *numerical study, J. Nanofluids*, 8 (2) 407-419 (2019).
23. Khan, Mair, et al. Heat transfer squeezed flow of Carreau fluid over a sensor surface with variable thermal conductivity: a numerical study. *Results in Physics* 6 (2016): 940-945.
24. Su, Xiaohong, and Yunxing Yin. Effects of an inclined magnetic field on the unsteady squeezing flow between parallel plates with suction/injection. *Journal of Magnetism and Magnetic Materials* 484 (2019): 266-271.
25. S.R. Mishra, MD. Shamshuddin, O. Anwar Bég and A. Kadir, Viscous dissipation and Joule heating effects in non-Fourier MHD squeezing flow, heat and mass transfer between Riga plates with thermal radiation: *variational parameter method solutions, Arabian J. Science Engineering,* 44, 8053–8066 (2019).
26. Zhou YS, Wang S, Yang Y, Zhu G, Niu S, Lin ZH, et al. Manipulating nanoscale contact electrification by an applied electric field. *Nano Letters*. **14** (3): 1567–72 (2014).
27. Noreen, S., and D. Tripathi. Heat transfer analysis on electroosmotic flow via peristaltic pumping in non-Darcy porous medium. *Thermal Science and Engineering Progress* 11 (2019): 254-262.
28. Azari, Milad, Arman Sadeghi, and Suman Chakraborty. Electroosmotic flow and heat transfer in a heterogeneous circular microchannel. *Applied Mathematical Modelling* 87 (2020): 640-654.

29. C. Zhao *et al.*, Electroviscous effects on the squeezing flow of thin electrolyte solution films, *Journal of Fluid Mechanics,*888, A29 (2020).
30. Bike, S. G. & Prieve, D. C. Electrohydrodynamic lubrication with thin double layers. *J. Colloid Interface Sci.* 136, 95–112 (1990).
31. Talapatra, S. & Chakraborty, S. Squeeze-flow electroosmotic pumping between charged parallel plates. *Intl J. Fluid Mech. Res.* 36, 460–472 (2009).
32. Bo, Z. & Umehara, N. Hydrodynamic lubrication theory considering electric double layer for very thin water film lubrication of ceramics. *JSME Intl J. C* 41, 285–290 (1998).
33. Liu, F., Klaassen, A., Zhao, C., Mugele, F. & van den Ende, D. Electroviscous dissipation in aqueous electrolyte films with overlapping electric double layers. *J. Phys. Chem. B* 122, 933–946 (2018).
34. J.C. Umavathi and O. Anwar Bég, Double diffusive convection in a dissipative electrically conducting nanofluid under orthogonal electrical and magnetic field: *a numerical study*, *Nanoscience and Technology: An International Journal*, 12 (2), 59-90 (2021).
35. Yang, Chunhong, Yongjun Jian, Zhiyong Xie, and Fengqin Li. Heat transfer characteristics of magnetohydrodynamic electroosmotic flow in a rectangular microchannel. *European Journal of Mechanics-B/Fluids* 74, 180-190 (2019).
36. Siva, T., S. Jangili, and B. Kumbhakar. Heat transfer analysis of MHD and electroosmotic flow of non-Newtonian fluid in a rotating microfluidic channel: an exact solution. *Applied Mathematics and Mechanics* (2021): 1-16 (2021).
37. K. Ramesh, D. Tripathi, M. M. Bhatti and C. M. Khalique, Electro-osmotic flow of hydromagnetic dusty viscoelastic fluids in a microchannel propagated by peristalsis. *Journal of Molecular Liquids* 314, 113568 (2020).
38. Santos E, Albo J, Irabien A. Magnetic ionic liquids: Synthesis, properties and applications. *RSC Advances,* **4** (75): 40008–40018 (2014).
39. Bombard A J F, Gonçalves F R, Shahrivar K, Ortiz A L, De Vicente J. Tribological behavior of ionic liquid-based magnetorheological fluids in steel and polymeric point contacts. *Tribol Int.*, **81**:309–320 (2015).
40. Okabe T, Moritaka D, Miyatake M, Kondo Y, Sasaki S, Yoshimoto S. Development and performance of a magnetic ionic liquid for use in vacuum-compatible non-contact seals. *Precis Eng.,* **47**: 97–103 (2017)

41. T. Thumma and V. M. Magagula. Transient electromagnetohydrodynamic radiative squeezing flow between two parallel Riga plates using a spectral local linearization approach. *Heat Transfer—Asian Research,* 49, no. 1 (2020): 67-85 (2020).
42. Seddeek, M.A. and Salama, F.A. The effects of temperature dependent viscosity and thermal conductivity on unsteady MHD convective heat transfer past a semi-infinite vertical porous moving plate with variable suction. *Computational Material Science*, Vol. 40 pp. 186-192 (2007).
43. Sadeghi, Arman, and Mohammad Hassan Saidi. Viscous dissipation effects on thermal transport characteristics of combined pressure and electroosmotically driven flow in microchannels. *International Journal Heat Mass Transfer* 53.19-20 (2010): 3782-3791.
44. Azari, Milad, Arman Sadeghi, and Suman Chakraborty. Graetz problem for combined pressure-driven and electroosmotic flow in microchannels with distributed wall heat flux. *International Journal Heat and Mass Transfer* 128 (2019): 150-160.
45. Saravani, Mahdi Sheikhizad, and Mohammad Kalteh. Heat transfer investigation of combined electroosmotic/pressure driven nanofluid flow in a microchannel: Effect of heterogeneous surface potential and slip boundary condition. *European Journal of Mechanics-B/Fluids* 80 (2020): 13-25.
46. Zhang, Jing-Kui, Ben-Wen Li, and Zhang-Mao Hu. Effects of optical parameters on fluid flow and heat transfer of participating magnetic fluid. *International Journal of Heat and Mass Transfer* 59 (2013): 126-136.
47. P.S. Gupta and A.S. Gupta, Squeezing flow between parallel plates, Wear, 45, 177-185 (1977).
48. K.C. Cramer and SI. Pai, *Magnetofluid Dynamics for Engineers and Applied Physicists*, MacGraw-Hill, New York, USA (1973).
49. Deng, Shuyan, Mingying Li, Ying Yang, and Tan Xiao. Heat transfer and entropy generation in two layered electroosmotic flow of power-law nanofluids through a microtube. *Applied Thermal Engineering* 196 (2021): 117314.
50. Rashidi, M. M., & Mohimanian Pour, S. A. (2010). A novel analytical solution of heat transfer of a micropolar fluid through a porous medium with radiation by DTM-Padé. *Heat Transfer—Asian Research*, *39*(8), 575-589.

51. Hassan, Hany, and Mohammad Mehdi Rashidi. An analytic solution of micropolar flow in a porous channel with mass injection using homotopy analysis method. *International Journal of Numerical Methods for Heat & Fluid Flow* (2014).

52. Rashidi, M. M., G. Domairry, and S. Dinarvand. The homotopy analysis method for explicit analytical solutions of Jaulent–Miodek equations. *Numerical Methods for Partial Differential Equations: An International Journal* 25, no. 2 (2009): 430-439.